Observation of Orbital-Selective Dual Modulations in an Anisotropic Antiferromagnetic Kagome Metal $TbTi_3Bi_4$

Renjie Zhang,[1,2,3] Bocheng Yu,[4] Hengxin Tan,[5] Yiwei Cheng,[6,1] Feiran Shen,[7] Junye Yang,[7] Dan Mu,[8] Xinru Han,[1,9] Alfred Zong,[10] Quanxin Hu,[1] Xuezhi Chen,[6,1] Yudong Hu,[1] Chengnuo Meng,[6] Junchao Ren,[6] Junqin Li,[6] Zhenhua Chen,[6] Zhengtai Liu,[6] Mao Ye,[6] Makoto Hashimoto,[11] Donghui Lu,[11] Shifeng Jin,[2,3] Binghai Yan,[12] Lunhua He,[2,7,13] Ziqiang Wang,[14] Tian Shang,[4,*] Yaobo Huang,[6,†] Baiqing Lv,[1,5,15,‡] and Hong Ding[1,16,17]

[1]*Tsung-Dao Lee Institute, Shanghai Jiao Tong University, Shanghai 200240, China*
[2]*Beijing National Laboratory for Condensed Matter Physics and Institute of Physics, Chinese Academy of Sciences, Beijing 100190, China*
[3]*University of Chinese Academy of Sciences, Beijing 100049, China*
[4]*Key Laboratory of Polar Materials and Devices (MOE), School of Physics and Electronic Science, East China Normal University, Shanghai 200241, China*
[5]*School of Physics and Astronomy, Shanghai Jiao Tong University, Shanghai 200240, China*
[6]*Shanghai Synchrotron Radiation Facility, Shanghai Advanced Research Institute, Chinese Academy of Sciences, Shanghai 201204, China*
[7]*Spallation Neutron Source Science Center, Dongguan 523803, China*
[8]*Institute for Quantum Science and Technology, Shanghai University, Shanghai 200444, China*
[9]*Department of Physics, Southern University of Science and Technology, Shenzhen 518055, China*
[10]*Departments of Physics and of Applied Physics, Stanford University, Stanford, California 94305, USA*
[11]*Stanford Synchrotron Radiation Lightsource, SLAC National Accelerator Laboratory, Menlo Park, California 94025, USA*
[12]*Department of Condensed Matter Physics, Weizmann Institute of Science, Rehovot 7610001, Israel*
[13]*Songshan Lake Materials Laboratory, Dongguan 523808, China*
[14]*Department of Physics, Boston College, Chestnut Hill, Massachusetts 02467, USA*
[15]*Zhangjiang Institute for Advanced Study, Shanghai Jiao Tong University, Shanghai 200240, China*
[16]*Hefei National Laboratory, Hefei 230088, China*
[17]*New Cornerstone Science Laboratory, Shanghai 201210, China*

(Received 23 September 2024; revised 19 April 2025; accepted 10 June 2025; published 10 July 2025)

Orbital selectivity is pivotal in dictating the phase diagrams of multiorbital systems, with prominent examples including the orbital-selective Mott phase and superconductivity. The intercalation of anisotropic layers represents an effective method for enhancing orbital selectivity and thereby shaping the low-energy physics of multiorbital systems. Despite its potential, related experimental studies, especially those elucidating the correlation between orbital selectivity and magnetism, remain limited. In this work, we systematically examine the interplay between orbital selectivity and magnetism in the newly discovered anisotropic kagome $TbTi_3Bi_4$ single crystal, and report the coexistence of orbital-selective dual-band modulations ($q_1 \sim 1/3a^*$, $q_2 \sim 0.28b^*$) within the antiferromagnetic (AFM) state. By combining soft x-ray and vacuum ultraviolet angle-resolved photoemission spectroscopy measurements, neutron powder diffraction, scanning tunneling microscopy, and density-functional-theory calculations, we identify these dual-band reconstructions as manifestations of the AFM order driven by a (approximately 1/3, 0.28, 0) nesting instability of the intercalated Tb $5d_{xz}$ orbitals. These orbital-selective modulations induce unusual momentum-dependent band folding and lead to the emergence of Dirac cones only at the $\bar{M}_1$ point, signaling a topological phase transition in the AFM state. Importantly, the discovery of orbital-selective (approximately 1/3, 0.28, 0) AFM order offers crucial insights into the mechanism underlying the fractional magnetization plateau in this kagome AFM metal. Our findings not only underscore the essential role of both conducting and localized electrons in determining the magnetic orders of $LnTi_3Bi_4$

*Contact author: tshang@phy.ecnu.edu.cn
†Contact author: huangyaobo@sari.ac.cn
‡Contact author: baiqing@sjtu.edu.cn

(Ln = lanthanide) kagome metals but also offer a pathway for manipulating magnetism through selective control of anisotropic electronic structures.

DOI: 10.1103/c3tg-1lxl

Subject Areas: Condensed Matter Physics, Magnetism, Materials Science

I. INTRODUCTION

In multiorbital systems, the interplay among different orbitals gives rise to a diverse range of quantum phases and emergent phenomena [1–4]. Orbital selectivity, a key feature of these systems, links specific orbitals to certain orders and quantum phases [3–5], including charge density wave (CDW), nematicity, and superconductivity. A crucial aspect of orbital selectivity is its connection with intrinsic anisotropy. For example, in transition-metal dichalcogenides and tetrachalcogenides [6–9], d-orbitals undergo orbital-selective reconstruction within the CDW states, where the resulting orbital textures are closely related to the anisotropy. Similarly, in cuprates, the highly anisotropic stripe phase is associated with distinct behaviors of the $2p_x$ and $2p_y$ orbitals of oxygen [10,11]. For nematicity in the iron-based superconductors, orbital-selective occupancy of electronic states is proposed to account for the orbital orders, resulting in electronic and structural anisotropies [4,12]. In the context of superconductivity, the orbital-selective pairings have been proposed to account for the anisotropic superconducting gap across different orbitals [13,14].

The above examples not only highlight the intricate role of orbital selectivity in determining the anisotropic correlated quantum phase, but also suggest an effective knob for manipulating the orbital characters through engineering anisotropic structures. Intuitively, introducing anisotropic structures, such as by intercalating layers, could modulate orbital distribution within the electronic structure, potentially enhancing orbital selectivity. More specifically, the anisotropic, low-dimensional Fermi surface that arises from selective orbitals might foster new correlated phases through mechanisms like Fermi surface nesting. As a result, it is anticipated that various correlated phases, including CDW and superconductivity, could emerge in anisotropic systems where orbital selectivity is significant [8,9,14]. However, the exploration of orbital selectivity and its correlation with other correlated quantum phases—especially magnetism—through the engineering of anisotropic structures, remains a relatively uncharted territory.

To understand the intricate relationship between orbital selectivity, anisotropy, and magnetic orders, we focus on a recently discovered kagome magnet, $TbTi_3Bi_4$, featuring double adjacent kagome layers interwoven with one-dimensional (1D) zigzag chains of Tb atoms [15–17]. The unique combination of magnetic rare-earth ions ($4f$ and $5d$ orbitals) and kagome layers (Ti $3d$ and Bi $6p$ orbitals), positions this family of compounds as a promising platform for exploring the interplay between orbital selectivity and anisotropy. Our systematic angle-resolved photoemission spectroscopy (ARPES) measurements reveal the coexistence of dual orbital-selective band modulations in the antiferromagnetic (AFM) state: a predominant band reconstruction along zigzag chains ($q_1 \sim 1/3a^*$) and a weaker band reconstruction perpendicular to the chains ($q_2 \sim 0.28b^*$). Through a comprehensive analysis of the folded bands and their temperature evolution corroborated by neutron power diffraction (NPD), scanning tunneling microscopy (STM), and density-functional-theory (DFT) calculations, we attribute these modulations to the Fermi-surface-nesting-driven AFM order. Crucially, the formation of AFM order gives rise to Dirac cones at the $\bar{M}_1$ point, pointing to a magnetic-order-induced topological phase transition. Following these observations, we propose a theoretical framework linking the $1/3$ a^* AFM phase to the unique $1/3$ magnetization plateau observed in this material. Our findings not only lay the groundwork for further exploration of orbital selectivity and magnetism in similar kagome magnets but also pave the way for tuning magnetism through the control of orbital selectivity and electronic structure.

II. RESULTS

$TbTi_3Bi_4$ crystallizes in space group *Fmmm* (no. 69) with lattice parameters $a = 5.8332$ Å, $b = 10.2792$ Å, and $c = 24.5883$ Å [Figs. 1(a) and 1(b)]. It shares the same structural motif as other members in the $LnTi_3Bi_4$ family, characterized by a slightly distorted Ti double kagome layer sandwiched between Tb-Bi double layers. Notably, the Tb atoms in these Tb-Bi layers form highly anisotropic quasi-1D zigzag chains that run parallel to the a axis. In addition, $TbTi_3Bi_4$ exhibits an exotic $1/3$ fractional magnetization plateau when applying the magnetic field along the zigzag chain, and showcases the topological-Hall-like features [17], suggesting the intricate interplay between the electronic structure and the magnetism.

To investigate such an interplay, we systematically performed magnetic and electrical characterizations, as well as ARPES measurements. As shown in Fig. 1(c), $TbTi_3Bi_4$ exhibits metallic behavior at low temperatures, with a distinct kink in the temperature-dependent electrical resistivity $\rho_{xx}(T)$ at $T_{N1} \sim 20.4$ K. Figure 1(d) displays the temperature dependence of magnetization $M(T)$ collected by applying magnetic fields along three different axes. For $H//a$, a sharp peak was observed at $T_{N1} = 20.4$ K in the $M(T)$, consistent with the resistivity data in Fig. 1(c), demonstrating the onset of AFM order in $TbTi_3Bi_4$ single

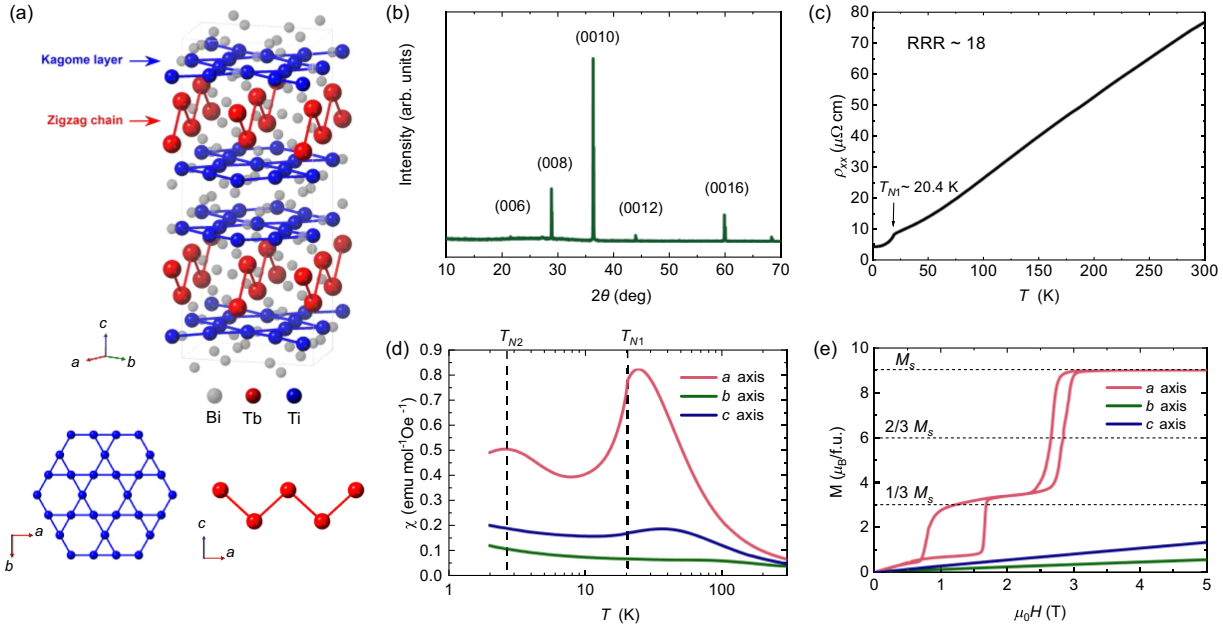

FIG. 1. Crystal structure and magnetism of $TbTi_3Bi_4$. (a) Crystal structure of $TbTi_3Bi_4$. The lower left and lower right panels show the kagome network and the intercalating zigzag chain of Tb, respectively. (b) The single-crystal x-ray diffraction of $TbTi_3Bi_4$. (c) The longitudinal electrical resistance along the a axis, showing the AFM transition at $T_{N1} \sim 20.4$ K. (d),(e) The temperature-dependent magnetic susceptibility (d) and the field-dependent magnetization (e) along the a, b, and c axes of $TbTi_3Bi_4$. T_{N1} and T_{N2}, in (d) represent the corresponding magnetic transition temperatures. M_S, $2/3M_S$, and $1/3M_S$ in (e) indicate different magnetization states, respectively. The weak kink at $2/3M_S$ relates to the $2/3$ magnetization plateau.

crystal. Furthermore, a humplike feature emerges at $T_{N2} \sim 2.5$ K in the susceptibility curve [Fig. 1(d)], indicative of a metamagnetic transition, consistent with other works [16,17].

Interestingly, the AFM transition is much less pronounced for either $H//b$ or $H//c$, implying a strong magnetic anisotropy in $TbTi_3Bi_4$ and suggesting that the Tb moments are predominantly aligned along the a axis, i.e., the direction of the zigzag chains, with much smaller components along other directions. Furthermore, the field-dependent magnetization $M(H)$ curves [Fig. 1(e)] reinforce the magnetic anisotropy, identifying the a axis as the easy axis while the b and c axes as the hard axes.

Uniquely, after undergoing a metamagnetic transition at approximately 1 T, there is a $1/3$ magnetization plateau in the field range of approximately 1 to 2.5 T in the $M(H)$ for $H//a$, as shown in Fig. 1(e). When the magnetic field exceeds approximately 3 T, the magnetization saturates, indicating the establishment of a forced ferromagnetic arrangement. Such metamagnetic transitions and magnetization plateau are absent for both $H//b$ and $H//c$. Magnetoresistance measurements (see Appendix A) further confirm the metamagnetic transitions observed in the $M(H)$ curves, and together with the $M(T)$ curves, they outline a rich magnetic phase diagram for $TbTi_3Bi_4$ (see Appendix A).

The observed highly anisotropic and intriguing magnetic properties are most likely due to the interplay between itinerant electrons and local magnetic moments of Tb $4f$ electrons. To elucidate the electronic structure of $TbTi_3Bi_4$, we performed DFT calculations. Figure 2 displays the calculated band dispersion at the $k_z = 0$ and $k_z = \pi$ planes (defined in the first Brillouin zone, or BZ, same as below). The calculations reveal several characteristic features for this kagome-lattice compound, including van Hove singularities (vHSs) and flat bands. Notably, the inequivalence of the vHSs at M_1/M_2 and L_1 highlights the anisotropy in the normal-state electronic structure, a trait commonly observed in the $LnTi_3Bi_4$ family [18,19]. Additionally, the observation of two closely spaced flat bands below the Fermi level (E_F) reflects the existence of double kagome layers within a single unit cell were identified [19]. Because of the presence of the rotation-symmetry-breaking intercalating layers, intrinsic strain, from the anisotropic structure, makes the Dirac point away from the high-symmetry point of the bulk BZ (K_1/K_2 and H_1/H_2) [20] and thus is absent in the DFT calculation results shown along the high-symmetry line.

To experimentally determine the electronic structure and understand its relationship with an intrinsic magnetic order, we continued to conduct ARPES measurements. We first mapped the Fermi surface within the k_x-k_y plane [Fig. 3(a)] and along the k_z direction [Fig. 3(b)] using both vacuum ultraviolet (VUV) light and soft x-ray (Appendix C). The consistency between the VUV and soft x-ray data demonstrates that our data predominantly represent bulk states. More specifically, from Fig. 3(b), one can see that the Fermi

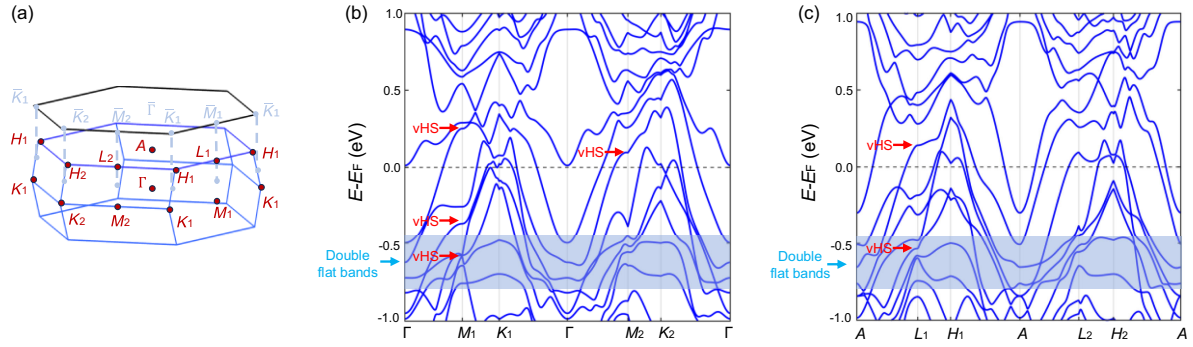

FIG. 2. The DFT calculation of the normal state. (a) Three-dimensional bulk BZ of $TbTi_3Bi_4$ (blue) and (001) projected surface BZ (black), with high-symmetry points indicated. (b),(c) The DFT-calculated band structure of non-magnetic bulk state along high-symmetry line in $k_z = 0$ (b) and $k_z = \pi$ (c) plane, with kagome features (vHSs, flat bands) indicated.

surface along the k_z direction appears nearly nondispersive. We interpret this as a result of both the quasi-two-dimensional nature of bands near the E_F and the k_z broadening [21].

Next, we focused on the ARPES measurements with VUV light to clarify the band structure near E_F. Starting from the center of the BZ, we identify two electronlike pockets forming two concentric circular Fermi surfaces (labeled α and α') around the $\bar{\Gamma}$ point [Figs. 3(a)–3(c)]. Note that the observed small splitting between α and α' is not seen in the DFT calculations (Fig. 2), and we attribute this splitting between α and α' to the surface effect caused by the self-doping of the non-neutral cleavage surface, which was commonly observed and well studied in AV_3Sb_5 (A = alkali metal) [22]. Next, we turn to the BZ corners $\bar{K}_1/\bar{K}_2$. At these points, there are pointlike Fermi pockets ϵ, which

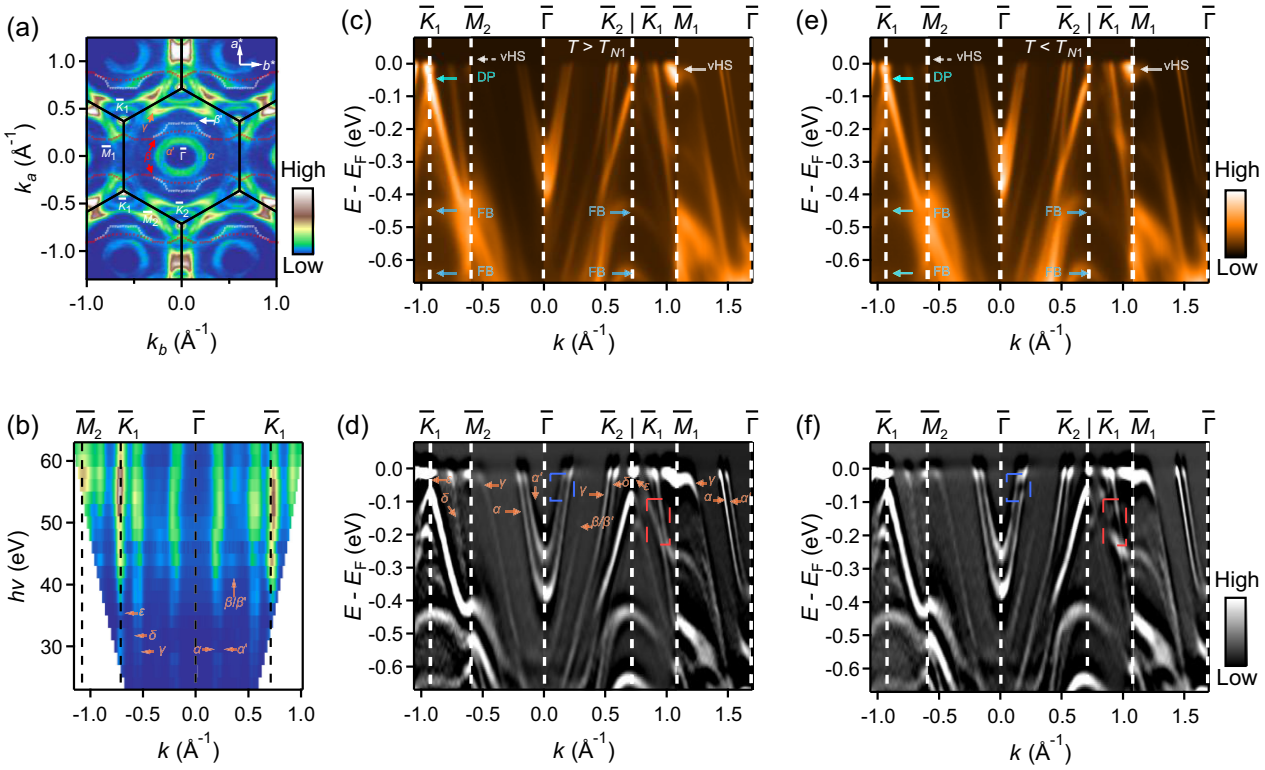

FIG. 3. The overall electronic structure of $TbTi_3Bi_4$ in the normal state and AFM state. (a) Fermi surface map of $TbTi_3Bi_4$ using VUV light of linear horizontal polarization (LH, parallel to the incident plane), at 100 eV. The red and white dotted lines are guides for the eye indicating the quasi-1D bands. (b) Photon-energy-dependent constant energy map along $\bar{M}_2 - \bar{K}_1 - \bar{\Gamma} - \bar{K}_1$. (c),(d) Intensity (c) and the corresponding curvature plots (d) of the band structure along the high-symmetry lines in the normal state ($T > T_{N1}$). DP means Dirac point, and FB means flat band. (e),(f) The same as (c) and (d), but taken in the AFM state ($T_{N2} < T < T_{N1}$). The blue dash rectangle and the red dashed rectangle in (d) and (f) indicate the band reconstruction.

are formed by the near-E_F Dirac point and can be clearly resolved in Figs. 3(c) and 3(d). In addition, a triangular holelike Fermi surface δ is seen around $\bar{K}_1/\bar{K}_2$ [Figs. 3(a), 3(c), and 3(d)].

Interestingly, as we move toward the $\bar{M}_1/\bar{M}_2$ points, vHSs near the E_F become distinctly observable. Akin to the AV_3Sb_5 family [23–28], bands emanating from the vHSs cross the E_F and form a large-γ pocket near the BZ boundary. However, the vHSs at $\bar{M}_1/\bar{M}_2$ are not equivalent due to the anisotropy of this material, leading to the warped Fermi surface [18,19,29,30], which deviates from the ideal nesting condition in the AV_3Sb_5 family [23–28]. This imperfect nesting between vHSs may explain the absence of CDW order in the kagome layer [25].

After the identification of the typical kagome features, our attention shifts to the characteristics of the Tb 1D zigzag chains. As shown in Fig. 3(a), from the Fermi surface map in the second BZ, one can identify a quasi-1D line perpendicular to the Tb chain direction (i.e., a^* direction). Detailed analysis (see Appendix E) reveals that this 1D line is formed by two quasi-1D Fermi surfaces β and β' denoted by red and white markers in Fig. 3(a), respectively. The β/β' bands have an electronlike dispersion parallel to the chain direction [Figs. 3(c) and 3(d)]. The presence of these quasi-1D β/β' pockets, supported also by the DFT calculations (see Appendix B for details), are key features of the 1D Tb chains.

Having established the electronic structure in the normal state, we now shift our focus to the AFM state. Figures 3(e) and 3(f) present the high-symmetry cuts in the AFM state ($T_{N2} < T < T_{N1}$). Compared with the normal-state results [Figs. 3(c) and 3(d)], we found that the kagome electronic features, including the vHSs, the Dirac points, and the flat bands, remain largely unaffected by the AFM order. On the other hand, when we turn our attention to the bands along the $\bar{K}_1 - \bar{M}_1$ path [highlighted by the red dashed rectangles in Figs. 3(d) and 3(f) aligned with the zigzag chain direction], we observe clear differences, suggesting the emergence of momentum-dependent band reconstruction in the AFM state.

To better visualize the band reconstruction, we systematically compared the measured high-resolution intensity and the corresponding curvature intensity plots along both $\bar{K}_1 - \bar{M}_1 - \bar{K}_1$ [Figs. 4(a) and 4(b)] and $\bar{K}_2 - \bar{M}_2 - \bar{K}_1$ directions [Figs. 4(c) and 4(d)]. Our findings are twofold. First, a distinct Dirac-cone-type crossing and some additional new states were observed along $\bar{K}_1 - \bar{M}_1 - \bar{K}_1$ direction below T_{N1}, as demonstrated by the red markers in Fig. 4(b)(ii) and the emergence of peak 3 in Fig. 4(g). Second, a suppression of the band intensity is noticeable in the energy range of approximately −0.1 to −0.2 eV along the $\bar{M}_1 - \bar{K}_1$ direction below T_{N1}, more clearly in the curvature intensity plot [highlighted by the black rectangle in Fig. 4(b)(i)]. In sharp contrast, despite these pronounced changes around $\bar{M}_1$, there is no distinct variation at $\bar{M}_2$ along the $\bar{K}_2 - \bar{M}_2 - \bar{K}_1$ direction [Figs. 4(c) and 4(d)] and $\bar{M}_2 - \bar{\Gamma} - \bar{M}_2$ (Appendix D, Fig. 14), underscoring the strong anisotropy and momentum dependence for the band reconstruction.

To be more precise, we extracted the dispersions of both the original bands in the normal state [indicated by gray lines in Fig. 4(a)] and the emergent Dirac bands in the AFM state [marked by red squares and diamonds in Fig. 4(b)(ii)]. Intriguingly, these emergent bands can be folded onto the original bands by a vector $q_1 \approx 0.36$ Å^{-1} [approximately $1/3a^*$, where $a^* = 2\pi/a$, as shown by the black arrows in Fig. 4(f)], suggesting the emergence of a density wave order associated with the vector q_1. Importantly, according to the irreducible representations of the little group at L_1 and M_1 in space group *Fmmm*, no symmetry-enforced degeneracies are expected at these points [31]. Thus, the emergent gapless Dirac point at the BZ boundary must either be protected by magnetic symmetries or originate from surface states induced by bulk band inversions. In either scenario, the presence of a Dirac-cone-like crossing points to an underlying topological state in the AFM phase.

Away from $\bar{M}_1$, the formation of the density wave order gives rise to hybridization gaps at crossing points of the folded bands, accounting for the suppression of spectral intensity in the region highlighted by the black rectangle in Fig. 4(b). Furthermore, a comparison between the experimentally observed reconstructed bands and the DFT-calculated k_z-projected band structure reveals that these reconstructions are predominantly concentrated in the $k_z = \pi$ plane. This suggests that the $k_z = \pi$ plane plays a particularly significant role in the band reconstruction process.

To further verify the band folding along a^*, we turn our attention to the electron pockets near the $\bar{\Gamma}$ point. The measured intensity plots above and below T_{N1} along the $\bar{\Gamma} - \bar{K}_2$ directions are summarized in Fig. 5. A gap of approximately 42.9 meV was observed on the outer band around $\bar{\Gamma}$, with obvious band backbending features [Figs. 5(e) and 5(f)]. As expected, the momentum separation of the left and right sides of the gapped outer band matches well with q_1. These observations reaffirm the existence of density wave modulations in $TbTi_3Bi_4$.

One of the predominating driving forces behind the density wave modulation is the Fermi surface nesting. In quasi-1D systems, the ideal nesting condition is often naturally present due to the prevalence of 1D Fermi surface. As demonstrated in Fig. 3(a) and Appendix E, $TbTi_3Bi_4$ hosts a quasi-1D Fermi surface β along $\bar{\Gamma}\bar{M}_1$ thanks to the intercalation of 1D Tb chains. Therefore, it is natural to link the density wave to the β Fermi surface. Indeed, from the mapped Fermi surfaces [Fig. 5(a)], one can see that the two branches of the β Fermi surface can be connected by a vector q_1 along a^*, strongly suggesting β as the underlying driving force for the observed density waves. Meanwhile,

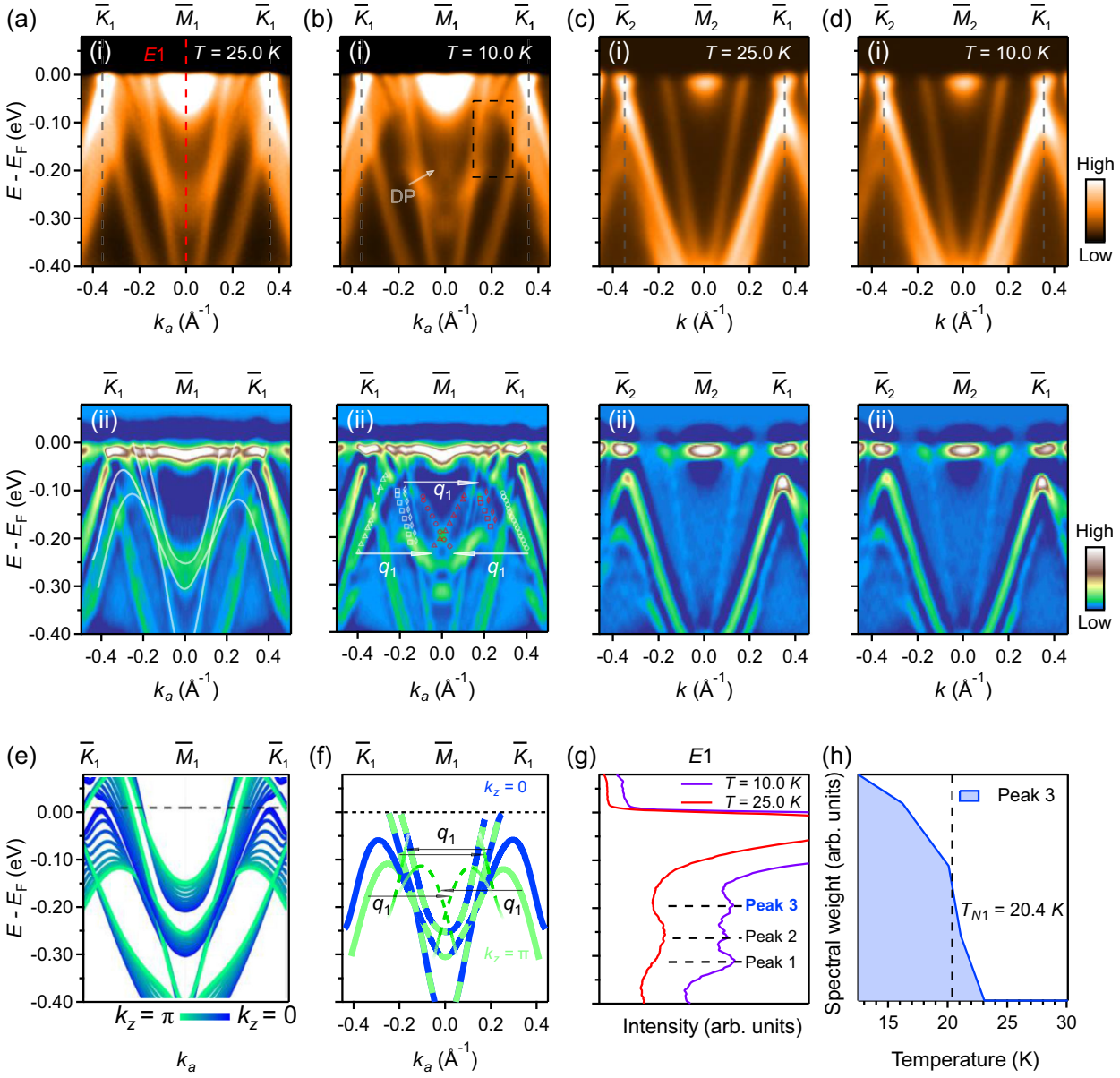

FIG. 4. Temperature dependence of the electronic band structure at $\bar{M}_1$ (along the a^* direction) and $\bar{M}_2$. (a) Intensity (i) and the corresponding curvature (ii) plots along the $\bar{K}_1 - \bar{M}_1 - \bar{K}_1$ direction in the normal state ($T = 25.0$ K). $E1$ indicates the EDC at $\bar{M}_1$, and the comparison with the EDC at $\bar{M}_1$ in the AFM state is shown in Fig. 4(g). (b) Same as (a), but taken in the AFM state ($T = 10.0$ K). The black dashed rectangle in (i) highlights the DOS suppression. DP in (i) represents the Dirac point. Red marks in (ii) indicate the folding bands, and white marks in (ii) are the respective original bands. The white arrow indicates the folding vector q_1. (c),(d) Same as (a) and (b), but taken along the $\bar{K}_2 - \bar{M}_2 - \bar{K}_1$ direction. (e) DFT calculation of k_z-projected band structure along $\bar{K}_1 - \bar{M}_1 - \bar{K}_1$ in the normal state. (f) Band dispersion extracted from (a), thick green and blue lines represent the $k_z = \pi$ and $k_z = 0$ bands, respectively. Green dashed lines represent folding bands. (g) EDCs taken from $\bar{M}_1$ (indicated by $E1$) in the intensity plots of (a) and (b). Peak 3 represents the Dirac crossing point. (h) Temperature evolution of the spectral weight of peak 3; data processing details are described in Appendix D.

one would expect the opening of an energy gap at the E_F for this β pocket. To this end, we performed a cut along β (see Appendix E). Comparing the AFM state with the normal state, we indeed find a gap opening of approximately 77.6 meV with respect to the E_F. The above observation is further supported by our DFT calculations. As shown in Fig. 5(b), a large, well-nested portion of quasi-one-dimensional Fermi surfaces is found under the wave vector q_1 in the $k_z = \pi$ plane, consistent with our ARPES results. These observations pin down that the anisotropic band reconstruction observed below T_{N1} is primarily driven by the nesting of quasi-1D Fermi surface.

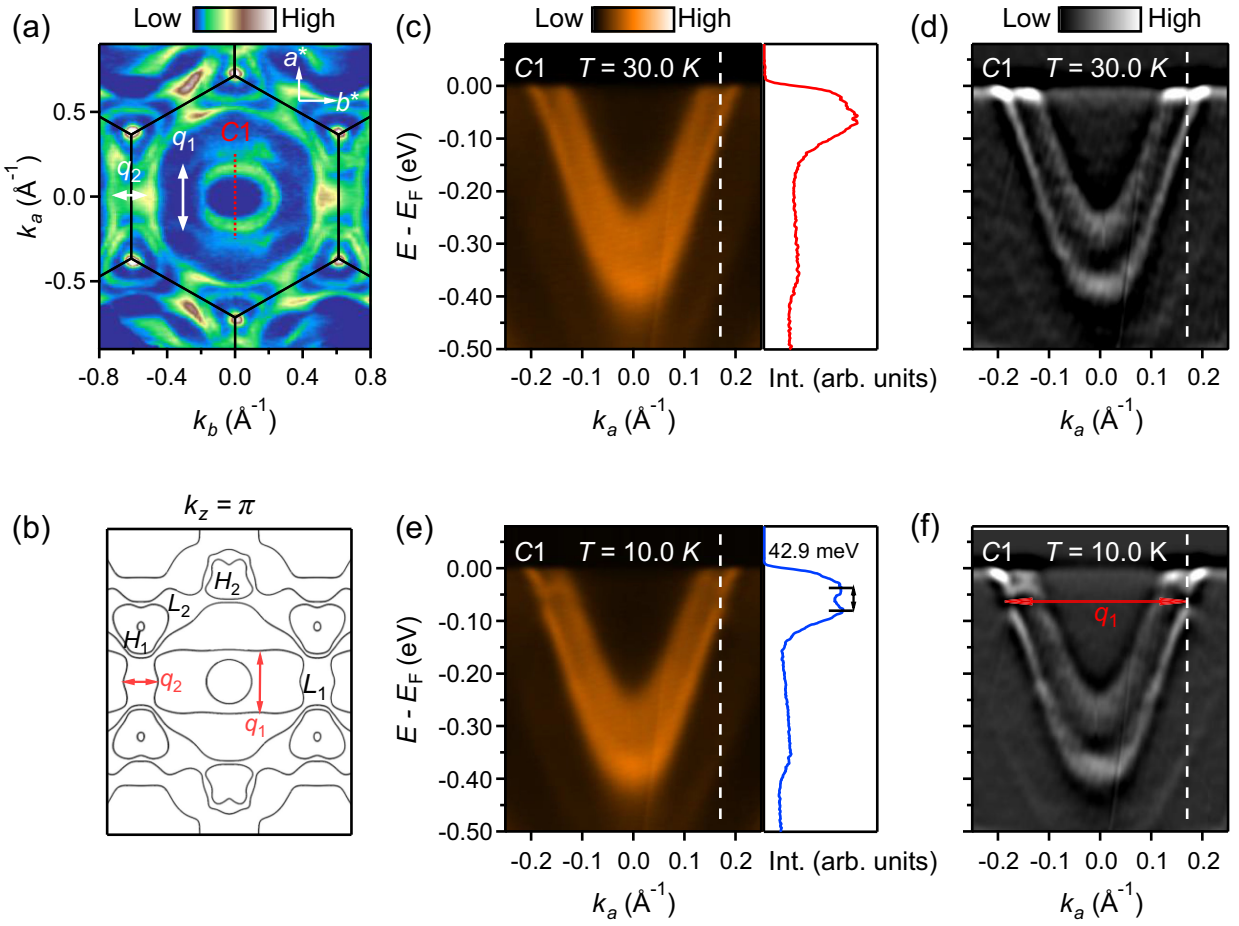

FIG. 5. Band folding around the $\bar{\Gamma}$ point. (a) Fermi surface map taken with photons of linear horizontal light (LH, parallel to the incident plane) + linear vertical light (LV, perpendicular to the incident plane) at 60 eV, with the red dashed line indicating the momentum location of cut $C1$ shown in (c)–(f), white arrows represent nesting vectors q_1 and q_2 connecting two pairs of parallel Fermi surfaces, respectively. (b) DFT-calculated Fermi surface in the $k_z = \pi$ plane. q_1, q_2 are identical to those shown in (a). (c),(d) Intensity (c) and the corresponding curvature (d) plots of the α/α' pockets ($T = 30.0$ K) taken along $C1$ [red line in (a)]. EDC at the white dash line is present in the right panel of (c). (e),(f) Same as (c) and (d), but taken at $T = 10.0$ K. Gap opening (approximately 42.9 meV) is visualized in the EDC shown in the right panel of (e).

After confirming the band reconstruction at specific points ($\bar{\Gamma}$ and $\bar{M}_1$) in the a direction, a natural question arises regarding the universality of Fermi surface nesting: Can it also occur in other directions? Notably, another pair of parallel Fermi surfaces exists around L_1 (projected onto $\bar{M}_1$ in a surface BZ) along a^* connected by wave vector q_2 [Figs. 5(a) and 5(b)]. To investigate the Fermi surface nesting in the b^* direction, we conducted a temperature-dependent ARPES measurement along $\bar{\Gamma}$-$\bar{M}_1$-$\bar{\Gamma}$ (Fig. 6). A comparison between Figs. 6(a) ($T > T_{N1}$) and 6(b) ($T < T_{N1}$) clearly reveals modifications in the energy bands around $\bar{M}_1$. Specifically, a notable change is the band folding associated with $q_2 = 0.28\ b^* (b^* = 2\pi/b)$ below T_{N1} [Figs. 6(b)(i) and 6(b)(ii)]. Interestingly, q_2 directly connects the nested Fermi surfaces near $\bar{M}_1$. Collaboratively, Fig. 6(b)(ii) exhibits a backbending feature in the near-E_F band at $\bar{M}_1$, in contrast to the normal-state band structure shown in Fig. 6(a)(ii). To better visualize the gap opening, we divided the spectra by a Fermi-Dirac function convolved with the experimental energy resolution [Figs. 6(a)(iii) and 6(b)(iii)]. A gap is clearly resolved only on the inner pocket centered at $\bar{M}_1$, whereas other near-E_F bands around $\bar{M}_1$ and $\bar{\Gamma}$ remain largely unaffected. This provides strong evidence for the existence of density wave order along $b*$.

To gain a comprehensive understanding of the electronic mechanism underlying band reconstruction near $\bar{M}_1$ along $\bar{\Gamma}$-$\bar{M}_1$-$\bar{\Gamma}$, we plotted k_z-projected band structure [Fig. 6(c)] and extracted the experimentally observed energy bands [Fig. 6(d)]. In line with the band reconstructions along $\bar{K}_1$-$\bar{M}_1$-$\bar{K}_1$ (Fig. 4), the primary modifications of energy bands along the b^* direction also mainly occur in the $k_z = \pi$ plane, where a well-nested rectangular quasi-1D Fermi surface is evident [Figs. 5(a) and 5(b)]. The

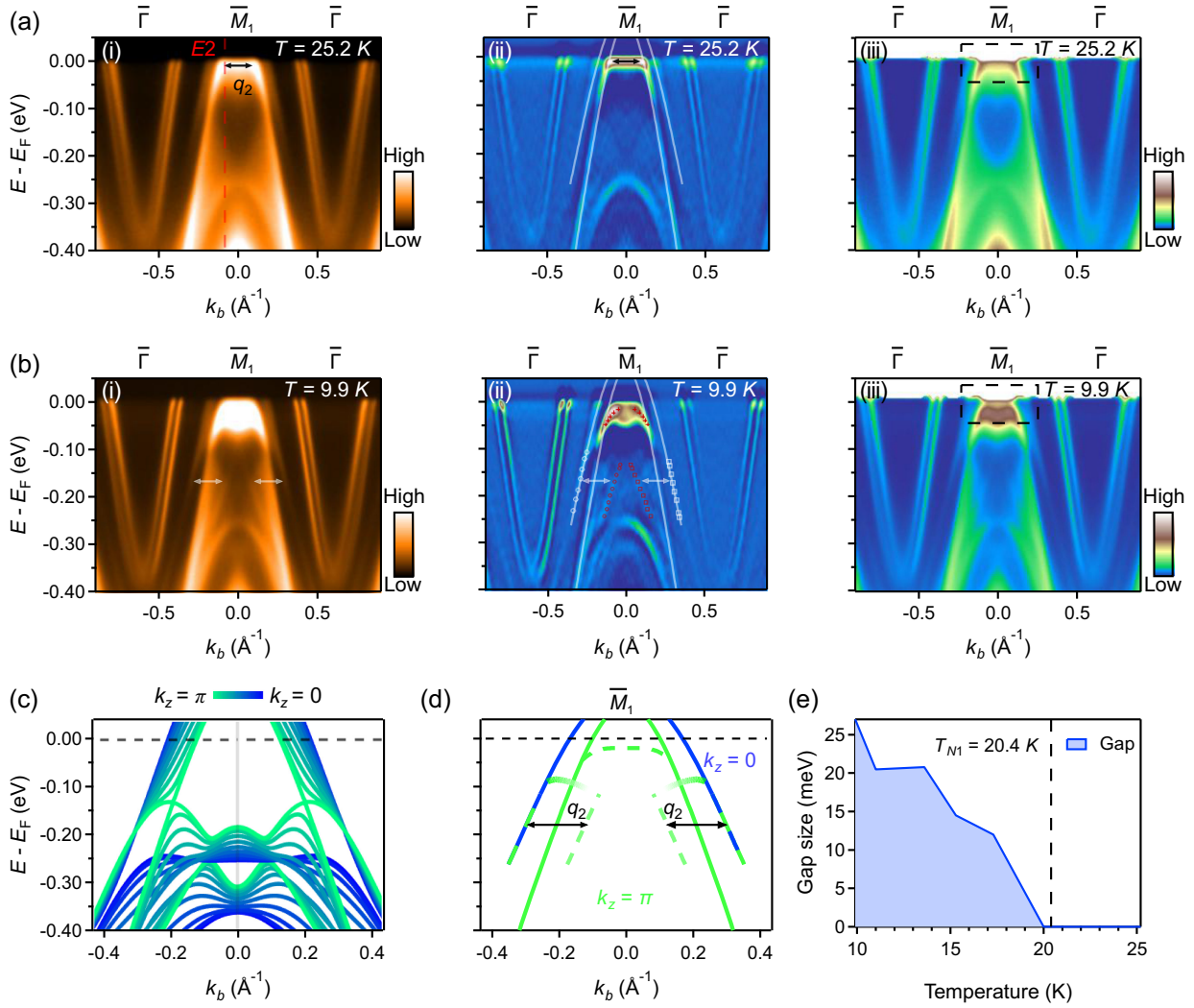

FIG. 6. Temperature dependence of the electronic band structure at $\bar{M}_1$ (along the b^* direction). (a) ARPES intensity plot (i), curvature plot (ii), and intensity plot divided by the Fermi-Dirac function convolved with energy resolution (iii), in the normal state ($T = 25.2$ K). The red dashed line in (i) indicates the EDC at the Fermi surface shown in (e). The arrow represents the wave vector q_2 connecting the Fermi surfaces. White curves in (ii) indicate the extracted energy bands near E_F. (b) Same as (a), but measured in the AFM state ($T = 9.9$ K). The white and red marks in (ii) represent the original and folding bands, respectively, connected by the folding vector q_2. The dashed rectangle box in (iii) highlights the gap opening due to the Fermi surface nesting. (c) k_z-projected band structure along $\bar{\Gamma}$-$\bar{M}_1$-$\bar{\Gamma}$, obtained from DFT calculation. (d) Band structure along $\bar{\Gamma}$-$\bar{M}_1$-$\bar{\Gamma}$, extracted from (a)(ii). Dashed curves indicate the reconstructed bands. (e) Temperature-dependent energy gap taken from symmetrized EDC of $E2$ in (a)(i).

symmetrized energy distribution curve (EDC) at k_F, marked as E2 in Fig. 6(a)(i) demonstrates that the gap on the Fermi surface in the AFM state ($T = 9.9$ K) is approximately 27 meV [Appendix D, Fig. 13(c)], lower than the corresponding gap value of 77.6 meV in the a^* direction (Appendix E), highlighting the strong anisotropy of the gap on the quasi-1D Fermi surface. Furthermore, Fig. 6(e) shows that the gap closing temperature is around 20.0 K, consistent with T_{N1}.

Given the multiorbital nature of $TbTi_3Bi_4$, understanding the orbital distribution is essential for comprehending the above discovery of momentum-dependent dual-band reconstructions. Since the band reconstruction is most pronounced in the $k_z = \pi$ plane [Figs. 4(e), 4(f), 6(c), and 6(d)] and along the quasi-1D Fermi surface, our analysis focuses on these features. Figure 7 and Appendix F summarize the DFT results on the orbital character. Interestingly, though the Ti-3d orbitals dominate the near-E_F energy bands (see Appendix F), the $5d_{xz}$ orbital (x and z align with the a and c axes, respectively) of Tb is closely tied to the reconstructed bands around L_1 ($\bar{M}_1$) and A ($\bar{\Gamma}$) below T_{N1} (Fig. 7). Notably, we observed that the $5d_{xz}$ orbital component is primarily concentrated on the portion of the quasi-1D Fermi surface parallel to the A-L_1($\bar{\Gamma}$-$\bar{M}_1$) direction, rather than being evenly distributed across the entire Fermi surface. This naturally explains

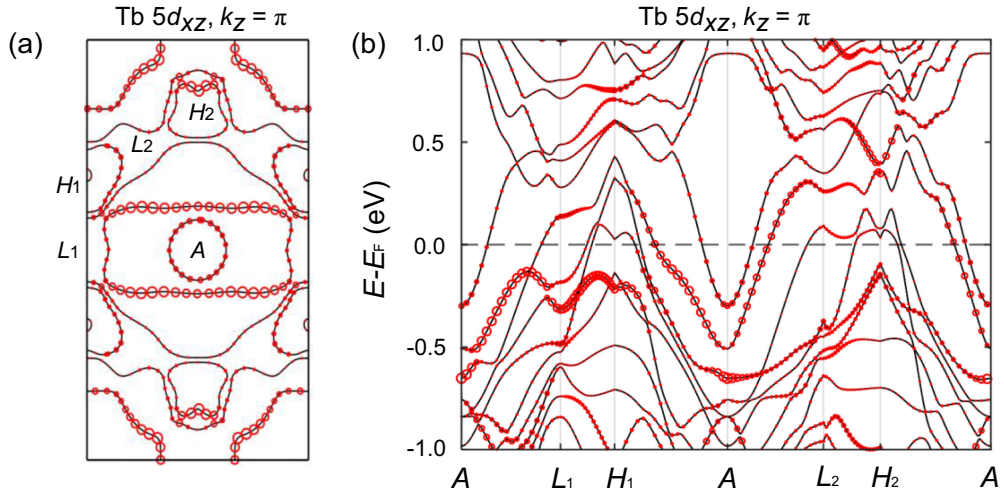

FIG. 7. DFT-calculated orbital distribution of Tb $5d_{xz}$. (a) DFT-calculated orbital distribution of Tb $5d_{xz}$ along the Fermi surface in the $k_z = \pi$ plane. (b) DFT-calculated orbital distribution of Tb $5d_{xz}$ in the energy band in the $k_z = \pi$ plane. The size of the red circles indicates the weight of Tb $5d_{xz}$; the black lines indicate the calculated Fermi surface (a) and the band structure (b), respectively.

the strong anisotropy in the gap along A-$H_2(\bar{\Gamma}$-$\bar{K}_1)$ and A-$L_1(\bar{\Gamma}$-$\bar{M}_1)$, demonstrating the anisotropic orbital-selective dual modulation in the AFM state. To experimentally verify the orbital characters, we conducted polarization-dependent ARPES measurements on the β band along both the $\bar{\Gamma}$-$\bar{K}_2$ and $\bar{\Gamma}$-$\bar{M}_1$ directions, which is compatible with DFT calculation results (Appendix G).

Given the consistency between the onset temperature of magnetic transition and band reconstruction, it is reasonable to associate the anisotropic Fermi surface nesting with the novel magnetism. To confirm this, we conducted NPD measurements both above and below T_{N1} to directly characterize the magnetic structure [Fig. 8(a)]. Evidently, new features emerge in the AFM phase, suggesting the emergence of a novel magnetic structure. Through Rietveld

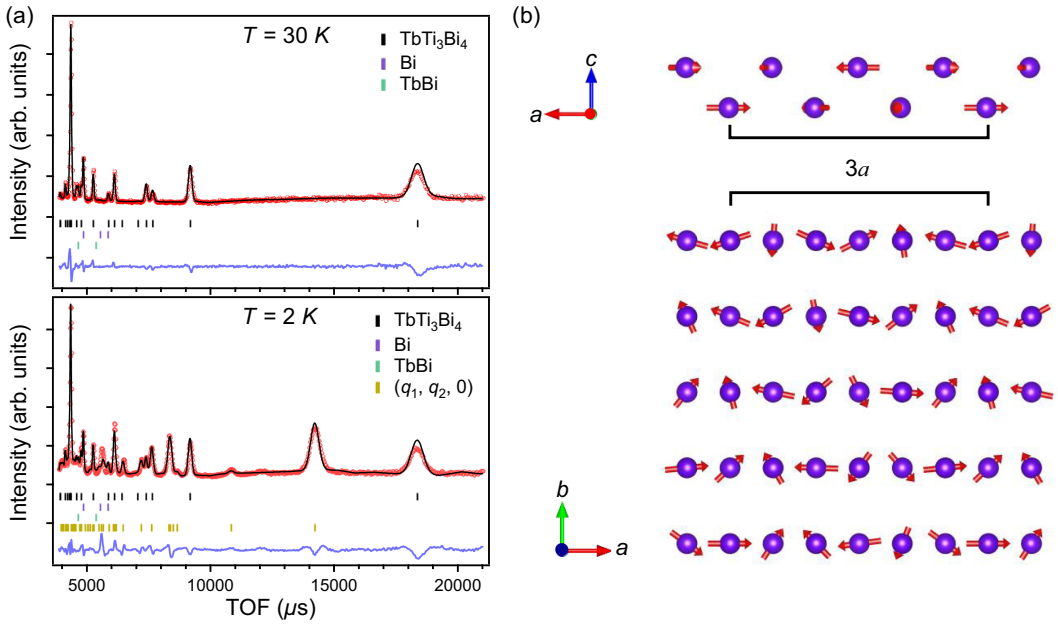

FIG. 8. NPD pattern and a possible magnetic structure corresponding to the vector (q_1, q_2, 0). (a) Upper and lower panel present the NPD pattern in the normal and AFM state, respectively. Black, purple, green, and yellow ticks represent the diffraction peak positions of $TbTi_3Bi_4$, Bi, TbBi, and (q_1, q_2, 0) magnetic structure, respectively. The blue lines at the bottom indicate the residual error between the fit and experimental results. (b) A proposed magnetic structure with magnetic vector (q_1, q_2, 0). Along the zigzag chain (a axis), the period is approximately 3a, while with an incommensurate arrangement of spins along the b axis. Top: zigzag chain of Tb, with approximate 3a period. Bottom: the Tb layer.

refinement of the NPD patterns, we found that the new peaks can be well described by a magnetic structure with a wave vector of $(q_1, q_2, 0)$, where $q_1 = 0.35a^* \sim 1/3a^*$ and $q_2 = 0.28b^*$. This wave vector is consistent with the nesting vector obtained from ARPES measurements. Additionally, our STM measurements performed above and below T_{N1} show no evidence of charge order with the wave vector $(1/3, 0.28, 0)$ (see Appendix H), thereby ruling out CDW order as the predominant order. Based on the wave vector (0.35, 0.28, 0) and the Rietveld refinement, we propose a possible magnetic structure characterized by an approximate triple period $(1/3a^*)$ along the a axis and an incommensurate arrangement along the b axis [Fig. 8(b)]. The moment magnitudes exhibit only weak, gradual modulation. We note that Fig. 8(b) presents one plausible solution derived from the NPD data; alternative magnetic configurations, e.g., spin helix, however, cannot be fully excluded.

III. DISCUSSION

Taken together, our temperature-dependent ARPES results, complemented by NPD, STM, and DFT calculations, reveal orbital-selective dual modulations in the band structure characterized by a wave vector of $(1/3, 0.28, 0)$ originated from an AFM state. The following key observations support this interpretation: (1) The onset of band reconstruction, such as the folding of Dirac bands [see peak 3 in Figs. 4(g) and 4(h)], occurs at the bulk AFM transition temperature ($T_{N1} \sim 20.4$ K). (2) NPD, which is sensitive to magnetic order, detects long-range magnetic ordering below T_{N1}. The observed magnetic structure shares the same wave vector as that of the Fermi surface nesting, strongly indicating an AFM state driven by electronic instability. (3) The reconstructed quasi-1D Fermi surface predominantly involves the $5d_{xz}$ orbitals of Tb atoms, which carry strong $4f$ magnetic moments and participate in the long-range AFM order. (4) STM measurements (see Appendix H) reveal no evidence of charge ordering or structural transitions with the modulation vector $(1/3, 0.28, 0)$, thereby confirming the magnetic origin of the orbital-selective modulation. Furthermore, a structural transition would typically induce folding across all electronic bands. However, bands near the $\bar{M}_2$ and $\bar{K}_1/\bar{K}_2$ points remain largely unaffected (Figs. 4 and 6), further supporting a magnetic, rather than structural, origin of the band reconstruction.

We now examine the key mechanisms driving the emergent magnetism in the $LnTi_3Bi_4$ family. First of all, the Ruderman-Kittel-Kasuya-Yosida (RKKY) interaction is a well-established mechanism for generating diverse magnetic ground states, including helical spin density waves and skyrmion lattices [32–34]. In the $LnTi_3Bi_4$ compounds, we demonstrate for the first time that RKKY interactions enhanced by quasi-1D Fermi surface nesting play a central role in determining the distinct magnetic behaviors observed across the series. As noted by Ortiz *et al.* [35], $EuTi_3Bi_4$ and $GdTi_3Bi_4$ contain magnetic ions with identical total angular momentum ($J = S = 7/2$), yet exhibit fundamentally different magnetic orders: $EuTi_3Bi_4$ is ferromagnetic, whereas $GdTi_3Bi_4$ displays antiferromagnetism with a $1/3$ magnetization plateau. This contrast correlates with their underlying electronic structures; $GdTi_3Bi_4$, like $TbTi_3Bi_4$, possesses a well-nested quasi-1D Fermi surface, while $EuTi_3Bi_4$ does not [29]. These findings demonstrate the critical role of Fermi surface geometry, particularly nesting instabilities, in mediating magnetic interactions. They further highlight low-dimensional structural motifs (e.g., zigzag chains) as promising design principles for engineering unconventional magnetic states.

In addition to Fermiology, orbital character plays an equally crucial role in shaping the magnetic behavior of the $LnTi_3Bi_4$ series. Within the framework proposed by Campbell [36], exchange interactions involving $4f$–$5d$ and $5d$–$5d$ (or $3d$–$5d$) orbitals are central to the magnetism of rare-earth transition-metal systems. Experimental studies on multiorbital interfaces, such as $LaAlO_3/EuTiO_3/SrTiO_3$ heterostructures, have revealed orbital-selective magnetic correlations [37], where the $3d_{xz/yz}$ orbitals mediate ferromagnetic coupling between Eu^{2+} ions, while the $3d_{xy}$ orbital promotes antiferromagnetic interactions. Complementary theoretical work has further emphasized the importance of orbital-dependent exchange in stabilizing skyrmion textures in Gd-based compounds [38]. In $TbTi_3Bi_4$, we reveal an orbital-selective dual modulation, in which the Tb $5d_{xz}$ orbital plays a direct role in establishing the antiferromagnetic ground state. This finding highlights the essential contribution of orbital degrees of freedom and supports the view that orbital selectivity, alongside Fermi surface nesting, is a key ingredient in driving the rich magnetism of the $LnTi_3Bi_4$ family.

Finally, it is worth noting that local $4f$ moments and their associated anisotropy shaped by the crystalline electric field (CEF) are indispensable to the full magnetic landscape of $LnTi_3Bi_4$. In $TbTi_3Bi_4$, the pronounced magnetization anisotropy has been attributed to strong CEF splitting of the Tb^{3+} ion levels. This stands in stark contrast to the nearly isotropic magnetic behavior in $GdTi_3Bi_4$, where the half-filled $4f$ shell minimizes CEF effects [15]. These observations demonstrate the necessity of incorporating CEF effects into any comprehensive understanding of magnetism in the $LnTi_3Bi_4$ series.

More importantly, the above analysis leads us to propose a plausible mechanism for explaining the $1/3$ fractional magnetization plateau based on the unique (0.35,0.28,0) AFM state. As illustrated in Fig. 8, the magnetic structure exhibits a special modulation along both the a and b axes, resulting in a two-dimensional configuration. However, as mentioned earlier, this system inherently possesses a dichotomy along the a and b axes in three key aspects:

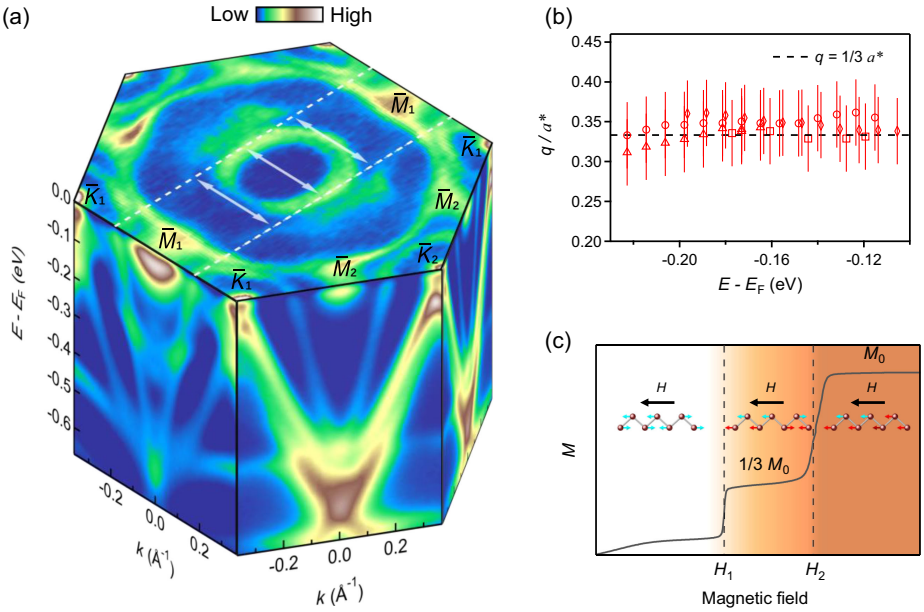

FIG. 9. Summary of electronic and magnetic properties of $TbTi_3Bi_4$. (a) Anisotropic electronic structure and reconstruction in the AFM state. White arrows indicate the nesting vector. The obvious anisotropic reconstruction is clearly visualized on the side surfaces of $\bar{M}_1$, and on the contrary, $\bar{M}_2$ does not show observable changes in the AFM state. (b) All the q vectors taken from Figs. 4(d) and 5(f). These vectors are approximately around $1/3\ a^*$; the error bar is estimated from the FWHM of the Dirac point in Fig. 4(b). (c) Schematic of the mechanism of the $1/3$ fractional magnetization plateau based on the $3a$ AFM state (intralayer coupling larger than interlayer coupling). Red colored arrows indicate the flipped spin; dark red arrows represent the spin flipped twice. H_1 and H_2 indicate the magnetic field of the metamagnetic transition.

First, the material has a quasi-1D lattice structure, which generates an anisotropic CEF that significantly impacts the local magnetic moments. Second, as shown by the magnetization behavior, $TbTi_3Bi_4$ exhibits an easy axis along the a axis, with much weaker magnetization along the b and c axes. More specifically, recent single-crystal neutron-diffraction measurements on $TbTi_3Bi_4$ reveal that the magnetic moments along the a axis are approximately 3 times larger than those along the b axis [17]. Third, in terms of the electronic structure, our ARPES measurements indicate that the energy gaps resulting from Fermi surface nesting along the a^* and b^* directions exhibit strong anisotropy. Similar to the magnetic moments observed by single-crystal neutron diffraction, the gap size along the a^* direction is approximately 3 times that along the b^* direction. Given the strong anisotropy in the lattice structure, magnetism, and electronic properties, we believe that the response of the AFM state to an external magnetic field is dramatically different along the a and b axes. The modulation associated with q_2 along the b axis (interchain) is likely suppressed when a field is applied along the a axis. Therefore, within a moderate field range (e.g., between 0 and H_1 in Fig. 9(c)), the moments along the b axis will be eliminated, and all magnetic moments will align or antialign along the a axis, maintaining a periodicity of approximately $3a$ along the a axis due to the relatively large gap in the q_1 modulation along the a^* direction. Although magnetic moments may exhibit some components along the c axis, we believe these are negligible and can be ignored. Since the q_1 vector is approximately $1/3\ a^*$, the possible magnetic structure should have a period of approximately $3a$ in real space. In this model [Fig. 9(c)], each zigzag chain constitutes of two layers of local moments. In each layer, moments are arranged as left-left-right (or right-right-left), with adjacent layers oriented oppositely. Assuming that intralayer coupling is stronger than the interlayer coupling (an alternative case is illustrated in Appendix I), an applied magnetic field exceeding H_1 first overcomes the nearest-neighbor magnetic coupling, and results in flips of all the spins in one layer to align with the adjacent layer, gaining energy through aligning a majority of local moments with the external field. This transition corresponds to the $1/3$ fractional plateau. As the magnetic field surpasses H_2, the remaining unflipped moments in two separated layers flip together [Fig. 9(c)] or flip one by one to align with the field (if the interlayer coupling is weaker than the intralayer coupling, these two ways are close in terms of energy), leading to saturation of magnetization or $2/3$ kink, respectively. This mechanism naturally explains the $1/3$ fractional magnetization plateau observed experimentally in the $1/3\ a^*$ AFM state, and also accounts for the weak kink in the magnetization curve reported recently [15,16]. Furthermore, during this spin-flip process, enhanced scattering of conduction

electrons is anticipated, leading to violent variations in both resistivity [Fig. 10(b), Appendix A] and Hall conductance [17]. Future neutron-diffraction experiments under applied magnetic fields are essential to confirm the proposed magnetic structure and test this scenario.

Given the possible close connection between the fractional magnetization plateau and the quasi-1D Fermi surface, our proposed mechanism can be experimentally tested by systematically tuning the Fermi surface via electrostatic gating or chemical doping, taking advantage of the RKKY interaction's sensitivity to the Fermi surface topology. Intriguingly, such a tuning could stabilize alternative magnetic ground states with different periodicities, potentially leading to fractional magnetization plateaus beyond the observed 1/3 value. More broadly, this mechanism offers a tunable platform for exploring novel phenomena associated with fractional magnetization plateaus in correlated electron systems.

IV. CONCLUSION

In conclusion, we present a comprehensive study of the electronic and magnetic structure of the anisotropic kagome magnet $TbTi_3Bi_4$, integrating ARPES measurements with NPD, STM, and DFT calculations. Our systematic temperature-dependent investigation in momentum space reveals a dual modulation of the band structure characterized by the wave vector (approximately 1/3, 0.28, 0) in the AFM state. Notably, the associated band folding leads to the formation of Dirac cones at the BZ boundary, hinting at the realization of magnetic-order-induced topological transition. By combining multiple experimental and theoretical approaches, we identify these dual-band reconstructions as manifestations of the AFM order driven by a (approximately 1/3, 0.28, 0) nesting instability. Very importantly, our DFT calculations demonstrate a direct correlation between the Tb $5d_{xz}$ orbital and the observed surprising momentum-dependent band reconstruction in the AFM state. This orbital-selective band reconstruction calls for further research into its potential role in the rich magnetic properties of $TbTi_3Bi_4$ and other materials in the $LnTi_3Bi_4$ family. Our finding provides key insights into the nature of the AFM state and the unusual fractional plateau of $TbTi_3Bi_4$, and opens avenues for manipulating magnetism through the orbital-selective control of the electronic structure.

V. METHODS

A. Single-crystal synthesis and sample characterization

$TbTi_3Bi_4$ single crystals were grown using a molten Bi flux method. High-purity Tb pieces (Thermo Fisher Scientific 99.9%), Ti granules (Thermo Fisher Scientific 99.99%), and Bi granules (Aladdin, 99.999%) in a ratio of 2:3:12 were loaded in an alumina crucible and sealed in a quartz ampule. Then, the quartz ampule was heated up to 1050 °C at a rate of 200 °C/h. After annealing at this temperature for more than 30 h, the ampule was slowly cooled down to 500 °C at a rate of 2 °C/h. After removing the excess Bi flux using a centrifuge, single crystals with typical dimension $2 \times 2 \times 0.5$ mm^3 were obtained, which showed a hexagonal shape.

The crystal structure of $TbTi_3Bi_4$ single crystals was checked via XRD at room temperature using an Empyrean x-ray diffractometer with Cu Kα radiation (Panalytical). Consistent with previous results, we confirm that our $TbTi_3Bi_4$ crystals crystallize in a centrosymmetric cubic structure (space group *Fmmm*, no. 69). The XRD measurements performed on a $TbTi_3Bi_4$ single crystal reveal a series of (00*l*) reflections [Fig. 1(b)], confirming the single-crystal nature of the $TbTi_3Bi_4$ sample and its *c* axis is perpendicular to the crystal plane.

Magnetization and electrical transport measurements were performed in a Quantum Design magnetic properties measurement system and physical property measurement system, respectively. For the resistivity measurements, the electric current was applied within the *a*-*b* plane, while the magnetic field was applied along the *c* axis.

B. ARPES measurement

ARPES measurements were performed at BL-09U and BL-03U of the Shanghai Synchrotron Radiation Facility (SSRF), and at BL 5-2 of the Stanford Synchrotron Radiation Lightsource (SSRL), all equipped with a SCIENTA Omicron DA30L analyzer. The energy resolution at BL-09U and BL-03U (SSRF) was 10–60 meV, with an angular resolution of 0.1°. The energy and angular resolutions at BL 5-2 (SSRL) were 5–20 meV and 0.1°, respectively. Samples were cleaved *in situ* and measured under a base vacuum better than 5×10^{-11} Torr.

C. DFT calculation

DFT calculations are performed within the Vienna *ab initio* simulation package [39]. The Perdew-Burke-Ernzerhof-type generalized-gradient approximation [40] is used to mimic the electronic-exchange-correlation interaction. The projector-augmented-wave potentials with nine valence electrons for Tb (*f* electrons are not considered), four valence electrons for Ti, and five valence electrons for Bi are employed. The crystal structure of $TbTi_3Bi_4$ is fully relaxed until the remaining force on all atoms is no larger than 1 meV/Å. The energy cutoff for the plane-wave basis set is 250 eV. A *k* mesh of $6 \times 6 \times 6$ is utilized to sample the reciprocal space. Spin-orbit coupling is considered for all calculations except for the structural relaxation. The Fermi surface is calculated by the Wannier Hamiltonian [41] extracted from DFT calculations with the basis set composed of Tb *d*, Ti *d*, and Bi *p* orbitals.

D. NPD measurement

NPD measurements were performed using the time-of-flight (TOF) diffractometer general-purpose powder diffractometer (GPPD) at the Chinese Spallation Neutron Source. The GPPD provides a high-intensity neutron beam with excellent spatial resolution, making it well suited for detailed analysis of complex magnetic structures. The sample was mounted in a vanadium holder and placed in a liquid-helium cryostat capable of reaching temperatures as low as 2 K. Diffraction patterns were collected in TOF mode over a wavelength range of 0.1–4.9 Å. The resulting NPD data were analyzed using the Rietveld refinement package within the FULLPROF suite.

ACKNOWLEDGMENTS

We are grateful to Chun Lin, Jianyang Ding, Jiayu Liu and Gexing Qu for their assistance with our ARPES measurements. We are also grateful to Mojun Pan for helpful discussions. B. L. acknowledges support from the Ministry of Science and Technology of China (Grant No. 2023YFA1407400), the National Natural Science Foundation of China (Grant No. 12374063), the Shanghai Natural Science Fund for Original Exploration Program (Grant No. 23ZR1479900), and the Cultivation Project of Shanghai Research Center for Quantum Sciences (Grant No. LZPY2024). H. D. acknowledges support from the Innovation Program for Quantum Science and Technology (Grant No. 2021ZD0302700), the New Cornerstone Science Foundation (Grant No. 23H010801236), and the National Natural Science Foundation of China (Grants No. 12488101). Y. B. H. acknowledges support by the Shanghai Committee of Science and Technology (Grant No. 23JC1403300), and the Shanghai Municipal Science and Technology Major Project. T. S. acknowledges support by the National Natural Science Foundation of China (Grants No. 12374105 and No. 12350710785), the Natural Science Foundation of Chongqing (Grant No. 2022NSCQ-MSX1468), and the Fundamental Research Funds for the Central Universities. Z. W. is supported by the U.S. Department of Energy, Basic Energy Sciences Grant No. DE-FG02-99ER45747. We acknowledge the technical support provided by the BL09U (31124.02.SSRF.BL09U) and BL03U (31124.02.SSRF.BL03U) beamlines at the Shanghai Synchrotron Radiation Facility (SSRF) for conducting the ARPES and PPMS measurements. Use of the Stanford Synchrotron Radiation Lightsource, SLAC National Accelerator Laboratory, is supported by the U.S. Department of Energy, Office of Science, Office of Basic Energy Sciences under Contract No. DE-AC02-76SF00515.

R. Z., B. Y., H. T., and Y. C. contributed equally to this work.

APPENDIX A: MAGNETIC CHARACTERIZATIONS

In the main text, we present transport measurements showing the magnetic transition of $TbTi_3Bi_4$. Additionally, we have conducted a systematic investigation of its magnetic properties by performing temperature-dependent magnetization measurements [Fig. 10(a)], field-dependent magnetoresistance measurements [Fig. 10(b)], and field-dependent magnetization measurements [Fig. 10(c)]. All measurements were taken with the magnetic field applied along the *a* axis, as shown in Fig. 10.

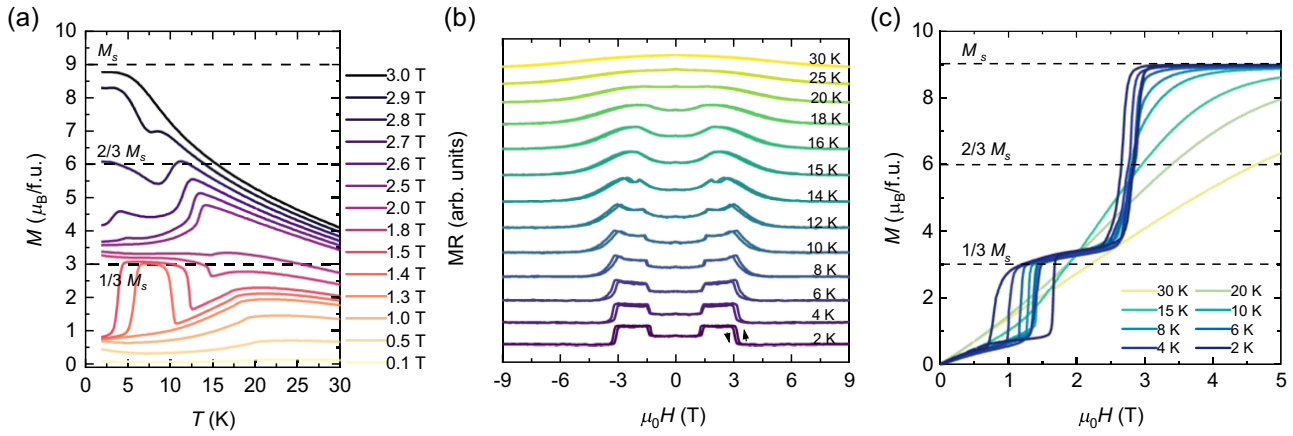

FIG. 10. Magnetic characterization and phase diagram of $TbTi_3Bi_4$. (a) Temperature-dependent magnetization under different fields along the *a* axis. (b) Temperature-dependent magnetoresistance from 2 to 30 K. (c) Magnetic-field-dependent magnetization from 2 to 30 K. These data were taken with a PPMS DynaCool at RIXS station of BL09U in SSRF.

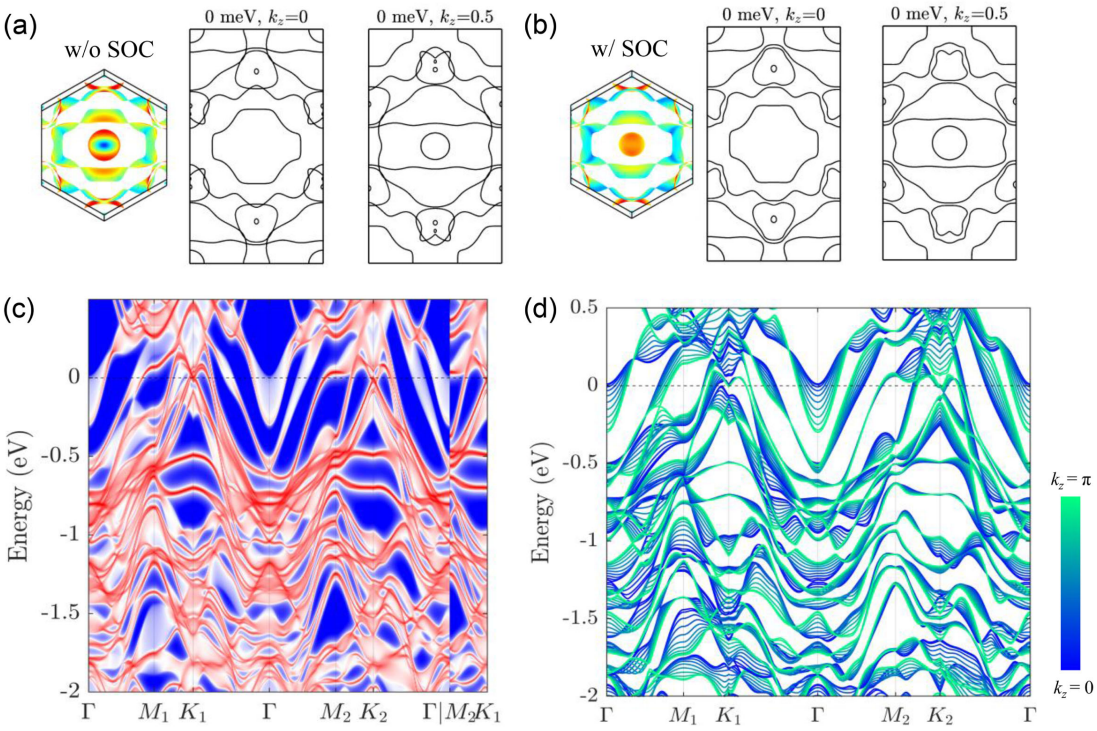

FIG. 11. DFT-calculated electronic structure. (a),(b) DFT calculation of the Fermi surface without (a) and with (b) SOC. The left panels in (a) and (b) are the k_z projection of bulk Fermi surfaces; the color scale indicates the Fermi velocity. The middle panels in (a) and (b) are the Fermi surfaces in the $k_z = 0$ plane. The right panels in (a) and (b) are the Fermi surfaces in the $k_z = \pi$ plane. (c) DFT calculation of Tb-Bi surface state. (d) DFT calculation of the k_z-integrated band structure.

APPENDIX B: DFT CALCULATION OF SURFACE PROJECTION OF BAND STRUCTURE AND FERMI SURFACES

In the main text of Fig. 2, we present the DFT calculation results for the band structure of the bulk state in the $k_z = 0$ and $k_z = \pi$ planes. To facilitate comparison with ARPES experimental data, we display the k_z-projected bulk Fermi surface, as well as the Fermi surface in the $k_z = 0$ and $k_z = \pi$ planes, both without spin-orbit coupling (SOC) [Fig. 11(a)] and with SOC [Fig. 11(b)]. Additionally, the DFT calculations for the Tb-Bi surface band structure and the k_z-projected bulk states are shown in Figs. 11(c) and 11(d), respectively.

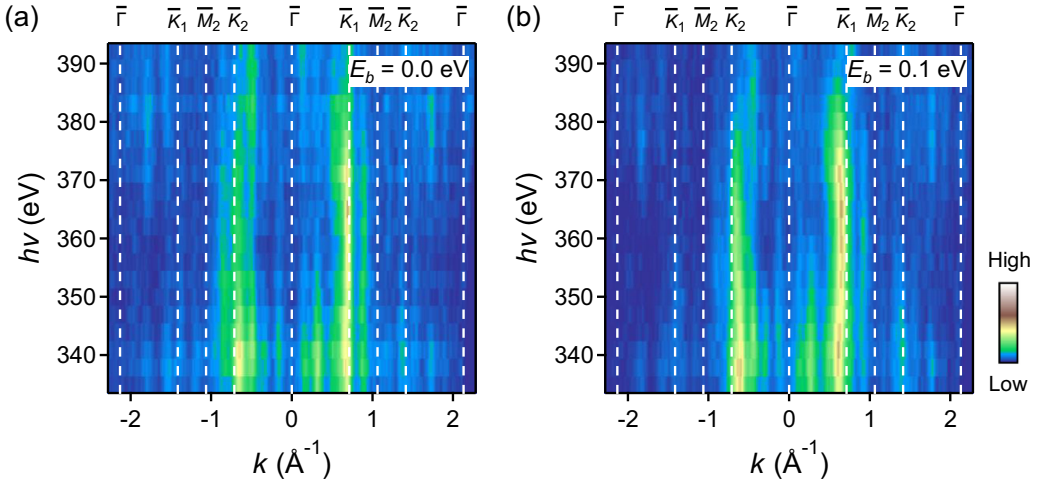

FIG. 12. Photon-energy-dependent soft x-ray ARPES. (a) Constant energy map at $E_b = 0.0$ eV. (b) constant energy map at $E_b = 0.1$ eV.

APPENDIX C: ARPES MEASUREMENT BY SOFT X-RAY

In Fig. 3(b) of the main text, we present the photon-energy-dependent Fermi surface measured by VUV-ARPES. To further confirm the nondispersive nature of the ARPES results along the k_z axis, we employed soft x-ray ARPES (335–392 eV) to obtain constant energy plots at $E_b = 0.0$ eV [Fig. 12(a)] and $E_b = 0.1$ eV [Fig. 12(b)]. Same as Fig. 3(b), from Fig. 10, one can see that the bands near E_F show minimal dispersion along k_z, suggesting that the observed states with VUV lights are mainly contributed by bulk states, but with a k_z broadening effect.

APPENDIX D: TEMPERATURE DEPENDENCE OF $\bar{M}_1/\bar{M}_2$

In the main text, we highlighted the differences in the $\bar{M}_1$ point cut along the a^* (Fig. 4) and b^* (Fig. 6) directions, between the AFM state and the normal state, and we also exhibited the temperature dependence of $\bar{M}_2$ along $\bar{K}_1$-$\bar{M}_2$-$\bar{K}_2$.

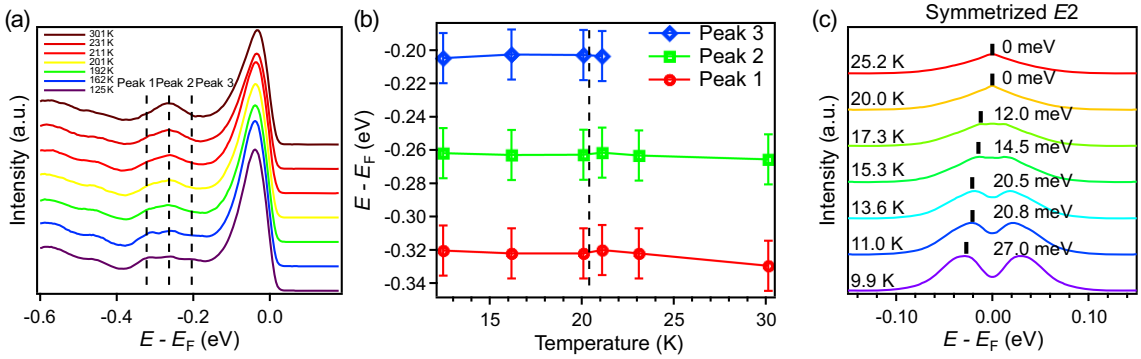

FIG. 13. Temperature dependence of the $\bar{M}_1$ point in the a^* and b^* directions. (a) EDC extracted from $\bar{M}_1$ at different temperatures. The definitions of peaks 1–3 are same as Fig. 4(g). (b) The temperature dependence of the peak positions of peaks 1–3. (c) Temperature dependence of the symmetrized EDC of $E2$ taken from Fig. 6(a)(i) in the b^* directions.

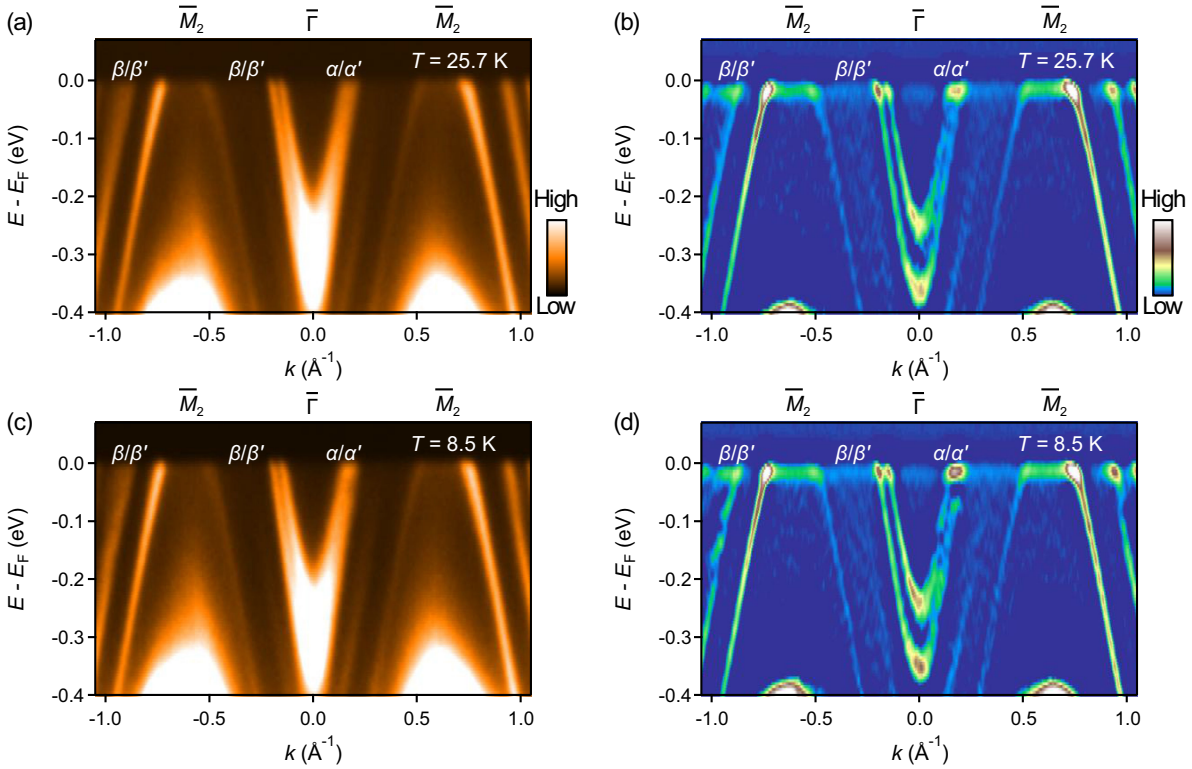

FIG. 14. Temperature dependence of $\bar{M}_2$ along $\bar{M}_2$-$\bar{\Gamma}$-$\bar{M}_2$. (a),(b) ARPES intensity plot and corresponding curvature plot taken at $T = 25.7$ K. (c),(d) Same as (a) and (b), but taken at $T = 8.5$ K.

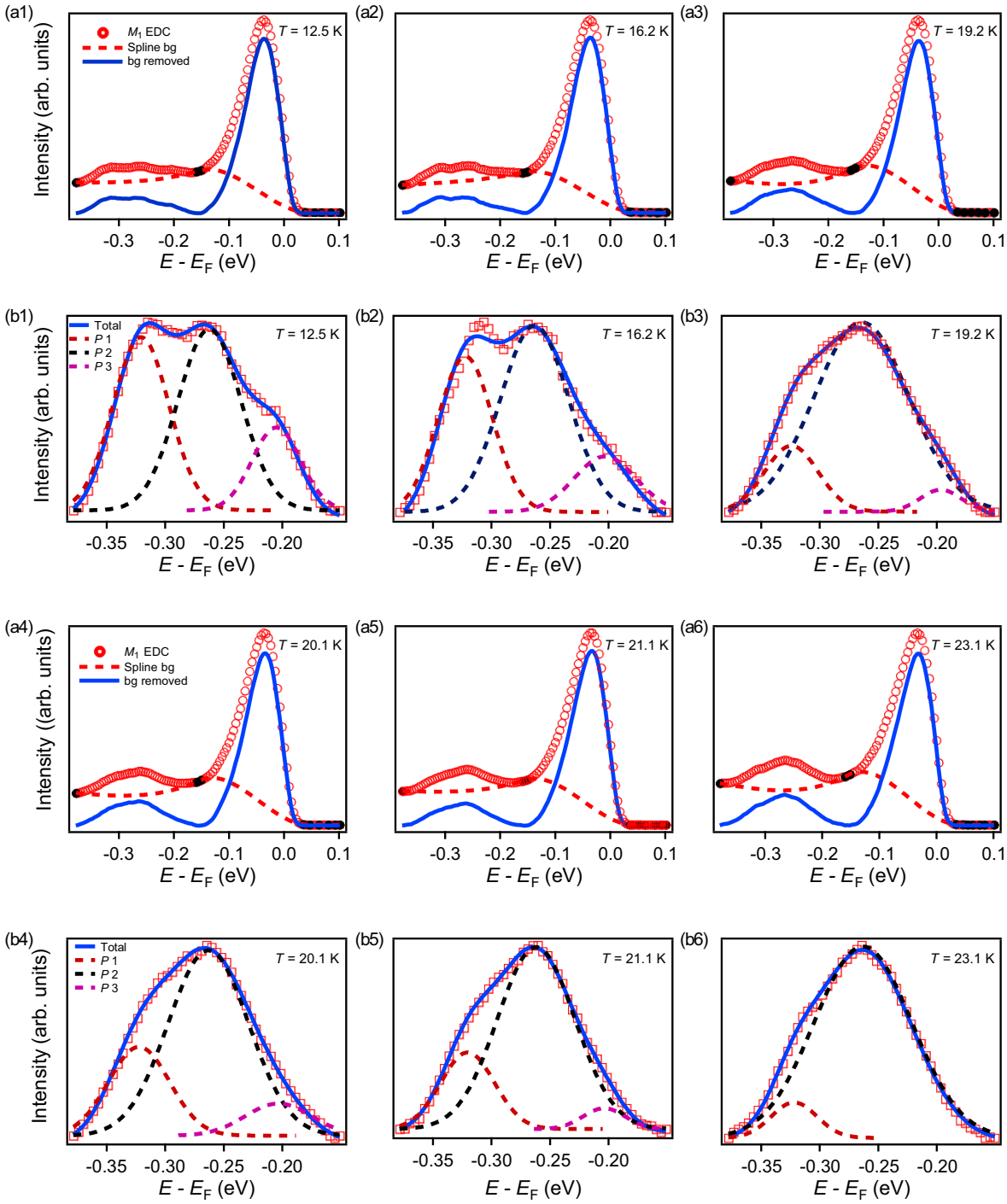

FIG. 15. The process to extract peaks in EDCs at $\bar{M}_1$. (a1)–(a6) Red dotted lines are raw EDCs at $\bar{M}_1$, red dashed lines are backgrounds obtained by cubic spline function interpolation, black dots are the fixed points for spline function interpolation, blue dashed lines are EDCs with backgrounds removed. (b1)–(b6) Fitting EDCs with the multiple Gaussian function. Square marks represent EDCs without backgrounds. Dashed curves are Gaussian-fitting results for each peak, and blue curves are the sum of each fitting curve. $P1$, $P2$, and $P3$ indicate peak 1, peak 2, and peak 3, respectively, in Figs. 4(g) and 11(a).

To provide a comprehensive description of the temperature-dependent behavior at the $\bar{M}_1/\bar{M}_2$ point, we present systematic data in Figs. 13 and 14. We applied a background subtraction using cubic spline interpolation and fitted the peaks with Gaussian functions (Fig. 15), enabling us to extract the spectral weight and peak positions for each peak.

It is evident that peak 3 emerges below T_N, while peaks 1 and 2 persist both above and below T_N. Furthermore, the energy positions of peaks 1–3 show no significant variation with the temperature [Figs. 13(a) and 13(b)].

The temperature-dependent symmetrized EDCs of $E2$ at k_F [Fig. 6(a)(i)] are presented in Fig. 13(c). At $T = 9.9$ K, the gap is approximately 27 meV, which is about one third of the gap observed in the a^* direction [Fig. 16(e)]. This significant difference highlights the strong anisotropy of the band reconstruction. The temperature at which the gap closes is approximately 20 K, which is consistent with T_{N1}, indicating that the band reconstruction is magnetically driven. The relationship between the gap opening in the b^* direction and antiferromagnetism is further confirmed by neutron powder diffraction, as discussed in the main text.

Because of the differences in band reconstruction at $\bar{M}_1$ along two perpendicular directions, we performed temperature-dependent ARPES measurements to thoroughly exclude the possibility of band reconstruction along the $\bar{\Gamma} - \bar{M}_2$ direction. These measurements reveal no noticeable change in the bands near $\bar{M}_2$ at low temperatures. However, the α/α' and β/β' bands exhibit kinklike reconstructions [Figs. 14(a) and 14(c)], which arise from band folding effects. These features are also evident in the curvature plots shown in Figs. 14(b) and 14(d).

APPENDIX E: TEMPERATURE DEPENDENCE OF QUASI-1D FERMI SURFACE PARALLEL WITH THE a AXIS

In the main text, we demonstrate the $1/3$ a^* band folding. Here, we further illustrate the gap opening on the quasi-1D Fermi surface, which is directly related to Fermi surface nesting. This supports the conclusion that the folding vector q originates from the nesting of the quasi-1D Fermi surface.

Figure 16(b) shows the splitting of β/β' near the $\bar{M}_1$ point. It is evident that β/β' exhibits stronger one dimensionality.

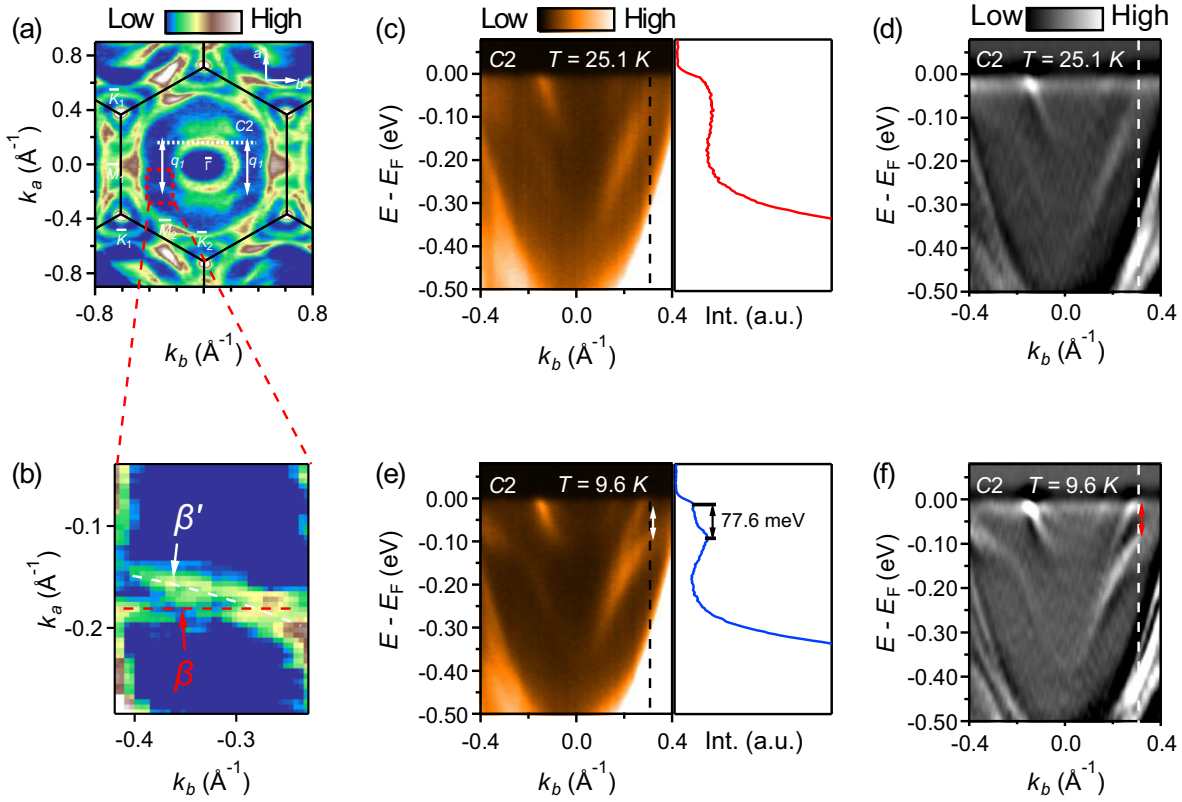

FIG. 16. Quasi-1D Fermi surface and gap opening related to the nesting. (a) Fermi surface map ($h\nu = 60$ eV, LH + LV). q represents the folding vector, and the white dashed line indicates the momentum location of the cut $C2$ in (c)–(f). (b) Enlargement of the Fermi surface β/β' [highlighted by the red dashed rectangle in (a)] with different color scales. (c),(d) Intensity plot (c) and curvature plot (d) of the cut along the quasi-1D Fermi surface [indicated by the white dashed line shown in (a)], taken at 25.1 K. (e),(f) Same as (c) and (d), but taken at 9.6 K, in the AFM state. The right panels of (c) and (e) present the EDCs taken at the dashed line indicated in (c) and (f).

APPENDIX F: DFT CALCULATIONS OF ORBITAL CHARACTER IN THE BAND STRUCTURE

We present the DFT calculation results for the Tb $5d$ [Figs. 17(a) and 17(c)] and Ti $3d$ [Figs. 17(b) and 17(d)] orbitals, projected onto the band structure along high-symmetry lines in the $k_z = 0$ [Figs. 17(a) and 17(b)] and $k_z = \pi$ planes [Figs. 17(c) and 17(d)]. Additionally, we show the orbital projections of the Tb $5d$ [Figs. 18(a) and 18(c)] and Ti $3d$ [Figs. 18(b) and 18(d)] orbitals on the Fermi surface in the $k_z = 0$ [Figs. 18(a) and 18(b)] and $k_z = \pi$ [Figs. 18(c) and 18(d)] planes.

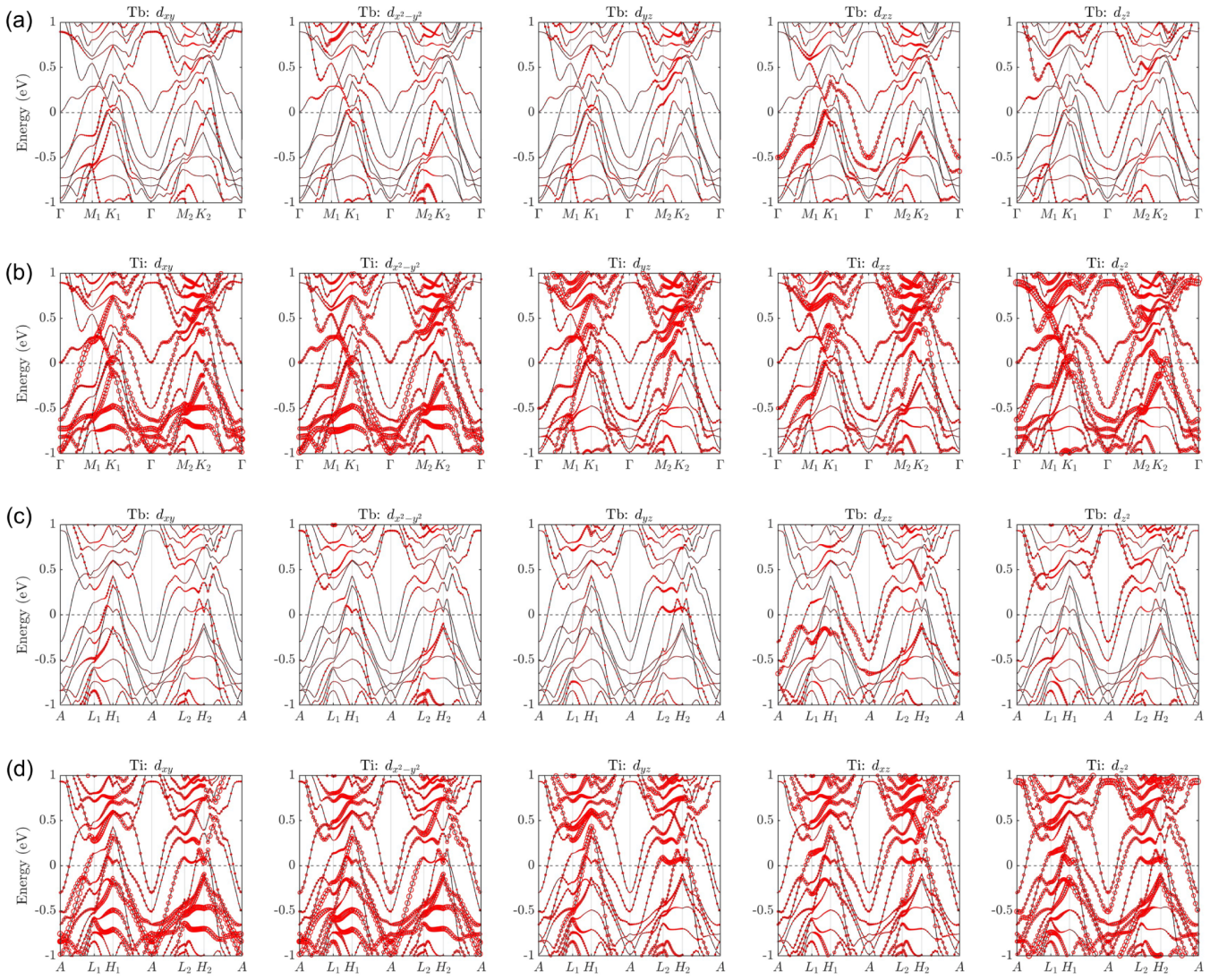

FIG. 17. DFT calculation of the orbital projection on energy bands. (a) Orbital projection of Tb $5d$ orbitals on energy bands in the $k_z = 0$ plane. (b) Orbital projection of the Ti $3d$ orbitals on the energy bands in the $k_z = 0$ plane. (c) Same as (a) but in the $k_z = \pi$ plane. (d) Same as (b) but in the $k_z = \pi$ plane. The size of the red circles indicates the weight of corresponding orbitals; the black lines indicate the calculated band structure.

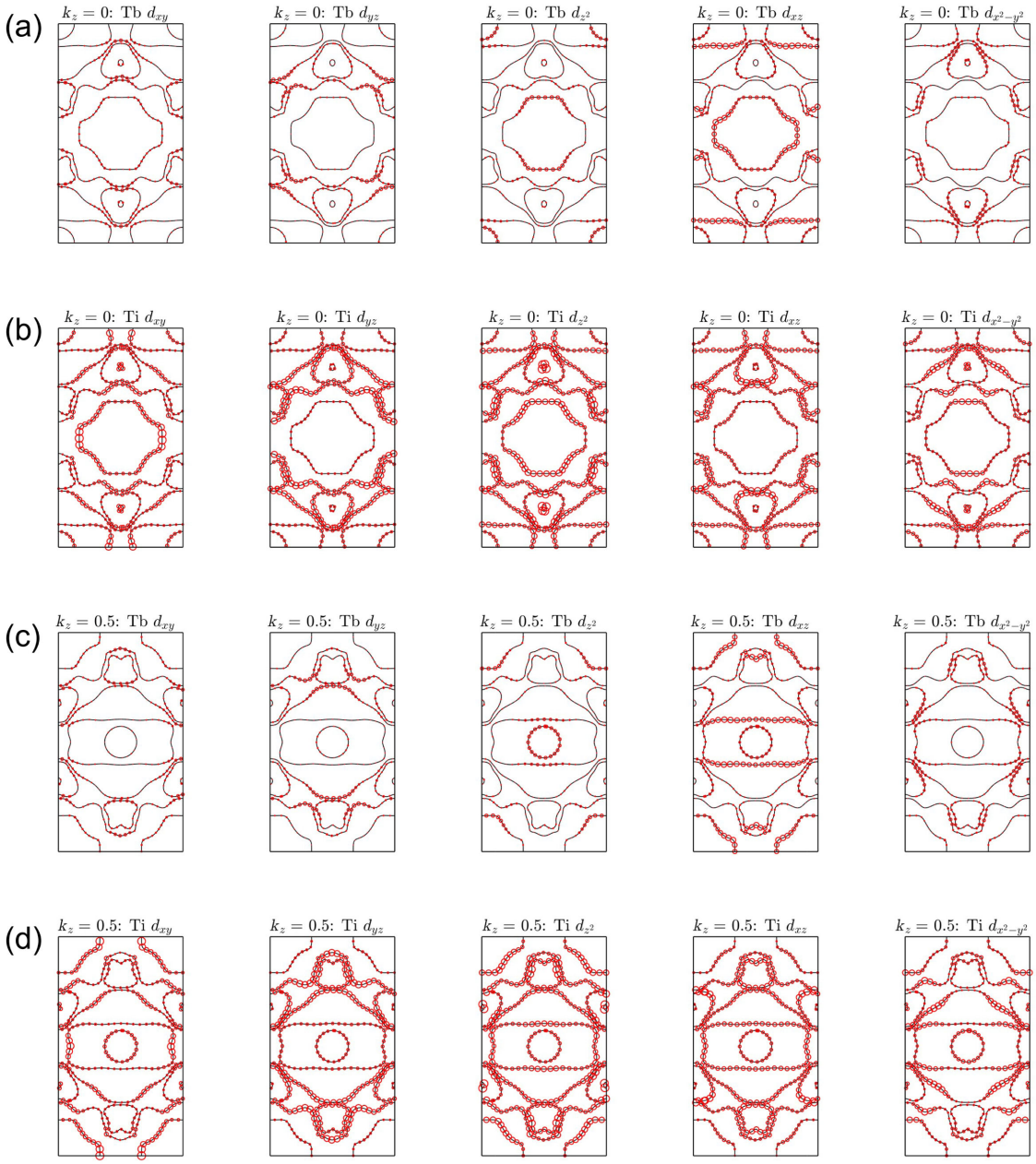

FIG. 18. DFT calculation of the orbital projection on Fermi surfaces. (a) Orbital projection of Tb $5d$ orbitals on Fermi surfaces in the $k_z = 0$ plane. (b) Orbital projection of the Ti $3d$ orbitals on Fermi surfaces in the $k_z = 0$ plane. (c) Same as (a), but in the $k_z = \pi$ plane. (d) Same as (b), but in the $k_z = \pi$ plane. The size of the red circles indicates the weight of corresponding orbitals; the black lines indicate the calculated Fermi surface.

APPENDIX G: POLARIZATION-DEPENDENT ARPES MEASUREMENTS AND ORBITAL ANALYSIS

In the main text, we analyze the orbital components of reconstructed energy bands in the AFM state based on an orbital-projected DFT calculation. Here, to support our theoretical analysis, we present polarization-dependent ARPES measurement results (Fig. 19). Because our main results come from β/β' bands, we focus on these bands below. Along $C3$ ($\bar{\Gamma}\bar{K}_2$) and $C4$ ($\bar{\Gamma}\bar{M}_1$) shown in Fig. 19(a), we used two kinds of polarization [LH and LV; the experimental setup is exhibited in Fig. 19(b)] to measure energy bands near E_F [Figs. 19(c)–19(f)]. It is clearly demonstrated that the β/β' bands show great differences under different conditions, which indicates the specific orbital characters of the β/β' bands. Along $\bar{\Gamma}\bar{K}_2$ (a axis), the β/β' bands are both observable under LH and LV polarization [Figs. 19(c) and 19(d)]. According to Tables I and II, the observable orbitals are d_{xz}, $d_{x^2-y^2}$, and d_{z^2}. DFT calculations show that the prominent orbitals

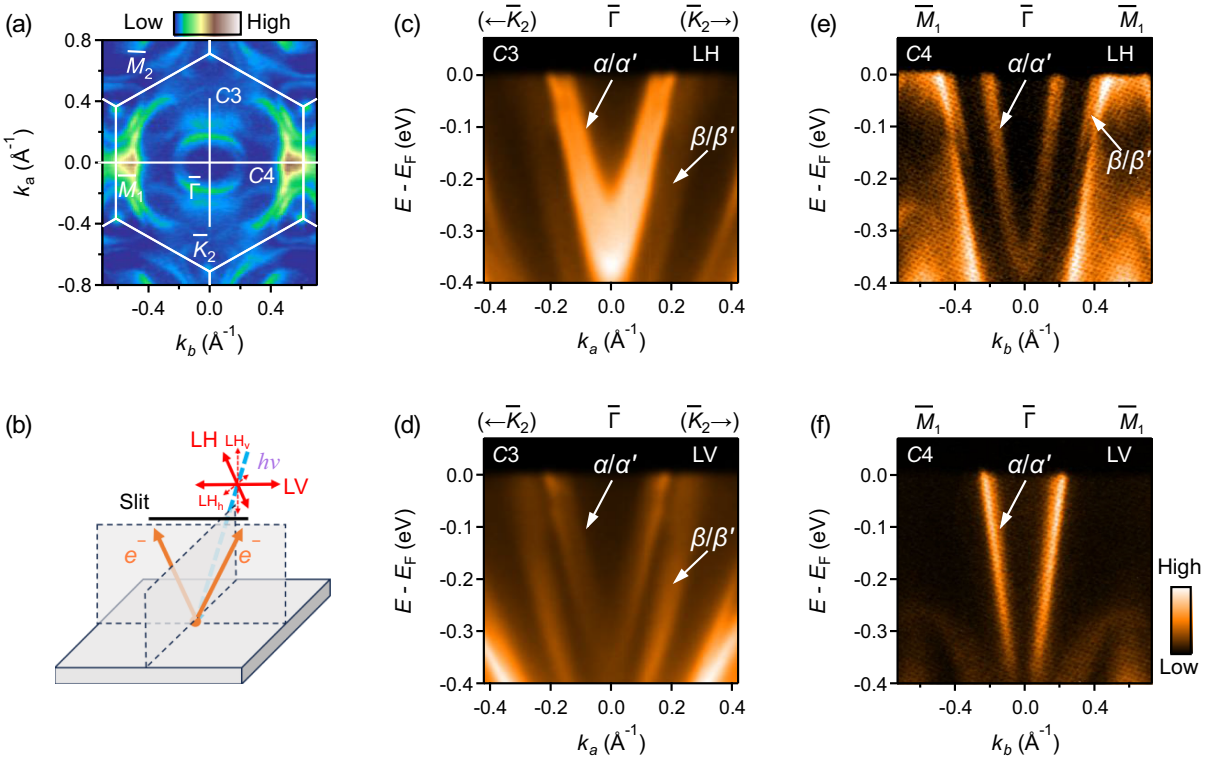

FIG. 19. Polarization-dependent ARPES measurements. (a) Fermi surface and indications of measurements cut ($C3$ and $C4$) in momentum space. $C3$ is along $\bar{\Gamma}\bar{K}_2$ (a axis), $C4$ is along $\bar{\Gamma}\bar{M}_1$ (b axis). (b) Schematic of the experimental geometry of our ARPES system. The plane of incident light is perpendicular to the emission plane. LV polarization is parallel with emission plane. LH polarization has two components; $\mathrm{LH_h}$($\mathrm{LH_v}$) is perpendicular (parallel) to the emission plane. (c),(d) ARPES intensity plot along $\bar{\Gamma}\bar{K}_2$ under LH (c) and LV (d) polarization. (e),(f) ARPES intensity plot along $\bar{\Gamma}\bar{M}_1$ under LH (e) and LV (f) polarization.

TABLE I. The parity of different orbitals along $\bar{\Gamma}\bar{M}_1$ and $\bar{\Gamma}\bar{K}_2$. $+$ indicates even parity, $-$ indicates odd parity.

	d_{xz}	d_{yz}	d_{xy}	$d_{x^2-y^2}$	d_{z^2}
$\bar{\Gamma}\bar{K}_2$	$+$	$-$	$-$	$+$	$+$
$\bar{\Gamma}\bar{M}_1$	$-$	$+$	$-$	$+$	$+$

TABLE II. Observable and nonobservable orbitals along $\bar{\Gamma}\bar{K}_2$ under LH ($\mathrm{LH_h}$ and $\mathrm{LH_v}$) and LV polarization. $\surd$ indicates observable orbitals, $\times$ indicates nonobservable orbitals.

$\bar{\Gamma}\bar{K}_2$	d_{xz}	d_{yz}	d_{xy}	$d_{x^2-y^2}$	d_{z^2}
$\mathrm{LH_h}$	$\times$	$\surd$	$\surd$	$\times$	$\times$
$\mathrm{LH_v}$	$\surd$	$\times$	$\times$	$\surd$	$\surd$
LV	$\surd$	$\times$	$\times$	$\surd$	$\surd$

TABLE III. Observable and nonobservable orbitals along $\bar{\Gamma}\bar{M}_1$ under LH ($\mathrm{LH_h}$ and $\mathrm{LH_v}$) and LV polarization. $\surd$ indicates observable orbitals, $\times$ indicates nonobservable orbitals.

$\bar{\Gamma}\bar{M}_1$	d_{xz}	d_{yz}	d_{xy}	$d_{x^2-y^2}$	d_{z^2}
$\mathrm{LH_h}$	$\surd$	$\times$	$\surd$	$\times$	$\times$
$\mathrm{LH_v}$	$\times$	$\surd$	$\times$	$\surd$	$\surd$
LV	$\times$	$\surd$	$\times$	$\surd$	$\surd$

on quasi-1D bands (β/β') are Tb d_{xz}, Ti d_{xz} and Ti d_{z^2} and Ti $d_{x^2-y^2}$, which are compatible with the experiment results. Next, we examine the bands along $\bar{\Gamma}\bar{M}_1$ (b^*). The β/β' bands are obvious under LH polarization [Fig. 19(e)], while they are hard to see under LV polarization [Fig. 19(f)]. According to the DFT results, Ti d_{xy} dominates the β/β' bands along $\bar{\Gamma}\bar{M}_1$, which is compatible with Tables I and III, where d_{xy} or d_{xz} is observable under LH polarization and is nonobservable under LV polarization. Above all, the polarization-dependent ARPES measurements support the orbital-projected DFT calculations. However, we note that due to the multiorbital nature of $TbTi_3Bi_4$, multiple orbitals with the same parity can contribute to a single band, making it challenging to solely determine the orbital character using polarization-dependent ARPES alone.

APPENDIX H: LATTICE STRUCTURE CHARACTERIZED BY STM BELOW AND ABOVE T_{N1}

In the main text, we use ARPES and NPD to characterize the electronic and magnetic structure below and above AFM transition temperature T_{N1}, and confirm that electronic band structure undergoes reconstruction accompanied by cooccurrence of a magnetic order below T_{N1},.

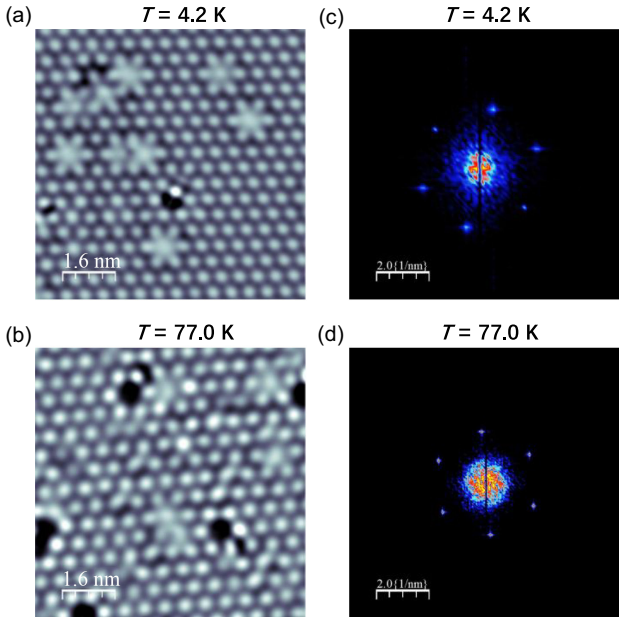

FIG. 20. Lattice structure of the $TbTi_3Bi_4$ surface characterized by STM. (a),(b) STM topography of $TbTi_3Bi_4$ taken below (a) and above (b) AFM transition temperature T_{N1}; (c), (d) Fourier transform of the topography shown in (a) and (b), respectively. Set point in (a): sample bias $V_s = 100$ mV, tunneling current $I_t = 100$ pA. Set point in (b): sample bias $V_s = 100$ mV, tunneling current $I_t = 300$ pA.

Importantly, the wave vector of Fermi surface nesting is the same as the emerging magnetic propagating vector. Here we performed STM measurements to further rule out a possible CDW or structure transition. We scan the large-scale area on the cleavage surface of $TbTi_3Bi_4$, and obtain the atom-resolved topography and the corresponding Fourier transform below [Figs. 20(a) and 20(c)] and above T_{N1}, [Figs. 20(b) and 20(d)]. The surface structure does not display modifications, but always exhibits the feature of the bulk structure.

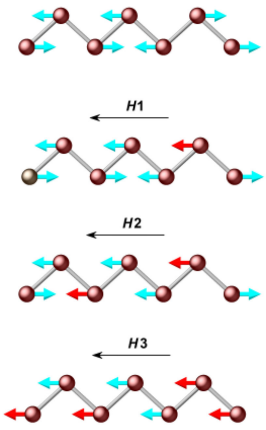

FIG. 21. the mechanism of 1/3 fractional magnetization plateau for interlayer coupling greater than intralayer coupling. Red colored arrows indicate flipped spins under magnetic field.

APPENDIX I: THE MECHANISM FOR THE FRACTIONAL MAGNETIZATION PLATEAU

In the main text, we consider the mechanism behind the 1/3 fractional plateau when the intralayer coupling is much stronger than the interlayer coupling. Here, we provide an alternative scenario where the interlayer coupling is dominant. In this case, for certain spins, it becomes energetically favorable to flip, leading to an antiparallel arrangement through the flipping of local moments, as illustrated in Fig. 21.

[1] G. R. Stewart, *Non-Fermi-liquid behavior in d- and f-electron metals*, Rev. Mod. Phys. **73**, 797 (2001).
[2] P. Gegenwart, Q. Si, and F. Steglich, *Quantum criticality in heavy-fermion metals*, Nat. Phys. **4**, 186 (2008).
[3] A. Georges, L. de' Medici, and J. Mravlje, *Strong correlations from Hund's coupling*, Annu. Rev. Condens. Matter Phys. **4**, 137 (2013).
[4] R. M. Fernandes, A. I. Coldea, H. Ding, I. R. Fisher, P. J. Hirschfeld, and G. Kotliar, *Iron pnictides and chalcogenides: A new paradigm for superconductivity*, Nature (London) **601**, 35 (2022).
[5] R. Yu, H. Hu, E. M. Nica, J.-X. Zhu, and Q. Si, *Orbital selectivity in electron correlations and superconducting pairing of iron-based superconductors*, Front. Phys. **9**, 578347 (2021).
[6] T. Ritschel, J. Trinckauf, K. Koepernik, B. Büchner, M. v Zimmermann, H. Berger, Y. I. Joe, P. Abbamonte, and J. Geck, *Orbital textures and charge density waves in transition metal dichalcogenides*, Nat. Phys. **11**, 328 (2015).
[7] M. D. Watson, O. J. Clark, F. Mazzola, I. Marković, V. Sunko, T. K. Kim, K. Rossnagel, and P. D. C. King, *Orbital- and k_z-selective hybridization of* Se 4*p and* Ti 3*d states in the charge density wave phase of* $TiSe_2$, Phys. Rev. Lett. **122**, 076404 (2019).
[8] N. Mitsuishi, Y. Sugita, M. S. Bahramy, M. Kamitani, T. Sonobe, M. Sakano, T. Shimojima, H. Takahashi, H. Sakai, K. Horiba, H. Kumigashira, K. Taguchi, K. Miyamoto, T. Okuda, S. Ishiwata, Y. Motome, and K. Ishizaka, *Switching of band inversion and topological surface states by charge density wave*, Nat. Commun. **11**, 2466 (2020).
[9] R. Z. Xu, X. Du, J. S. Zhou, X. Gu, Q. Q. Zhang, Y. D. Li, W. X. Zhao, F. W. Zheng, M. Arita, K. Shimada, T. K. Kim, C. Cacho, Y. F. Guo, Z. K. Liu, Y. L. Chen, and L. X. Yang, *Orbital-selective charge-density wave in* $TaTe_4$, npj Quantum Mater. **8**, 44 (2023).
[10] K. Fujita, M. H. Hamidian, S. D. Edkins, C. K. Kim, Y. Kohsaka, M. Azuma, M. Takano, H. Takagi, H. Eisaki, S. Uchida, A. Allais, M. J. Lawler, E.-A. Kim, S. Sachdev, and J. C. S. Davis, *Direct phase-sensitive identification of a d-form factor density wave in underdoped cuprates*, Proc. Natl. Acad. Sci. U.S.A. **111**, E3026 (2014).
[11] R. Comin, R. Sutarto, F. He, E. H. da Silva Neto, L. Chauviere, A. Fraño, R. Liang, W. N. Hardy, D. A. Bonn, Y. Yoshida, H. Eisaki, A. J. Achkar, D. G. Hawthorn, B. Keimer, G. A. Sawatzky, and A. Damascelli, *Symmetry of charge order in cuprates*, Nat. Mater. **14**, 796 (2015).

[12] R. M. Fernandes, A. V. Chubukov, and J. Schmalian, *What drives nematic order in iron-based superconductors?*, Nat. Phys. **10**, 97 (2014).

[13] R. Yu, J.-X. Zhu, and Q. Si, *Orbital-selective superconductivity, gap anisotropy, and spin resonance excitations in a multiorbital* t-J_1-J_2 *model for iron pnictides*, Phys. Rev. B **89**, 024509 (2014).

[14] P. O. Sprau, A. Kostin, A. Kreisel, A. E. Böhmer, V. Taufour, P. C. Canfield, S. Mukherjee, P. J. Hirschfeld, B. M. Andersen, and J. C. S. Davis, *Discovery of orbital-selective Cooper pairing in* FeSe, Science **357**, 75 (2017).

[15] K. Guo, Z. Ma, H. Liu, Z. Wu, J. Wang, Y. Shi, Y. Li, and S. Jia, *1/3 and other magnetization plateaus in the quasi-one-dimensional Ising magnet* $TbTi_3Bi_4$ *with zigzag spin chain*, Phys. Rev. B **110**, 064416 (2024).

[16] B. R. Ortiz, H. Zhang, K. Górnicka, D. S. Parker, G. D. Samolyuk, F. Yang, H. Miao, Q. Lu, R. G. Moore, A. F. May, and M. A. McGuire, *Intricate magnetic landscape in antiferromagnetic kagome metal* $TbTi_3Bi_4$ *and interplay with* $Ln_{2-x}Ti_{6+x}Bi_9$ $(Ln: Tb \cdots Lu)$ *shurikagome metals*, Chem. Mater. **36**, 8002 (2024).

[17] E. Cheng *et al.*, *Spectroscopic origin of giant anomalous Hall effect in an interwoven magnetic kagome metal*, arXiv:2405.16831.

[18] Z. Jiang, T. Li, J. Yuan, Z. Liu, Z. Cao, S. Cho, M. Shu, Y. Yang, Z. Li, J. Liu, J. Ding, Z. Liu, J. Liu, J. Ma, Z. Sun, X. Wan, Y. Guo, D. Shen, and D. Feng, *Topological surface states in quasi-two-dimensional magnetic kagome metal* $EuTi_3Bi_4$, Sci. Bull. **69**, 3192 (2024).

[19] Y. Hu, C. Le, L. Chen, H. Deng, Y. Zhou, N. C. Plumb, M. Radovic, R. Thomale, A. P. Schnyder, J.-X. Yin, G. Wang, X. Wu, and M. Shi, *Magnetic coupled electronic landscape in bilayer-distorted titanium-based kagome metals*, Phys. Rev. B **110**, L121114 (2024).

[20] C. Si, Z. Sun, and F. Liu, *Strain engineering of graphene: A review*, Nanoscale **8**, 3207 (2016).

[21] V. N. Strocov, *Intrinsic accuracy in 3-dimensional photoemission band mapping*, J. Electron Spectrosc. Relat. Phenom. **130**, 65 (2003).

[22] T. Kato, Y. Li, M. Liu, K. Nakayama, Z. Wang, S. Souma, M. Kitamura, K. Horiba, H. Kumigashira, T. Takahashi, Y. Yao, and T. Sato, *Surface-termination-dependent electronic states in kagome superconductors* AV_3Sb_5 $(A = K, Rb, Cs)$ *studied by micro-ARPES*, Phys. Rev. B **107**, 245143 (2023).

[23] Z. Liu, N. Zhao, Q. Yin, C. Gong, Z. Tu, M. Li, W. Song, Z. Liu, D. Shen, Y. Huang, K. Liu, H. Lei, and S. Wang, *Charge-density-wave-induced bands renormalization and energy gaps in a kagome superconductor* RbV_3Sb_5, Phys. Rev. X **11**, 041010 (2021).

[24] S. Cho, H. Ma, W. Xia, Y. Yang, Z. Liu, Z. Huang, Z. Jiang, X. Lu, J. Liu, Z. Liu, J. Li, J. Wang, Y. Liu, J. Jia, Y. Guo, J. Liu, and D. Shen, *Emergence of new van Hove singularities in the charge density wave state of a topological kagome metal* RbV_3Sb_5, Phys. Rev. Lett. **127**, 236401 (2021).

[25] M. Kang, S. Fang, J.-K. Kim, B. R. Ortiz, S. H. Ryu, J. Kim, J. Yoo, G. Sangiovanni, D. Di Sante, B.-G. Park, C. Jozwiak, A. Bostwick, E. Rotenberg, E. Kaxiras, S. D. Wilson, J.-H. Park, and R. Comin, *Twofold van Hove singularity and origin of charge order in topological kagome superconductor* CsV_3Sb_5, Nat. Phys. **18**, 301 (2022).

[26] Y. Hu, X. Wu, B. R. Ortiz, S. Ju, X. Han, J. Ma, N. C. Plumb, M. Radovic, R. Thomale, S. D. Wilson, A. P. Schnyder, and M. Shi, *Rich nature of van Hove singularities in kagome superconductor* CsV_3Sb_5, Nat. Commun. **13**, 2220 (2022).

[27] H. Luo *et al.*, *Electronic nature of charge density wave and electron-phonon coupling in kagome superconductor* KV_3Sb_5, Nat. Commun. **13**, 273 (2022).

[28] T. Kato, Y. Li, T. Kawakami, M. Liu, K. Nakayama, Z. Wang, A. Moriya, K. Tanaka, T. Takahashi, Y. Yao, and T. Sato, *Three-dimensional energy gap and origin of charge-density wave in kagome superconductor* KV_3Sb_5, Commun. Mater. **3**, 1 (2022).

[29] J. Guo *et al.*, *Tunable magnetism and band structure in kagome materials* $RETi_3Bi_4$ *family with weak interlayer interactions*, Sci. Bull. **69**, 2660 (2024).

[30] Z. Zheng, L. Chen, X. Ji, Y. Zhou, G. Qu, M. Hu, Y. Huang, H. Weng, T. Qian, and G. Wang, *Anisotropic magnetism and band evolution induced by ferromagnetic phase transition in titanium-based kagome ferromagnet* $SmTi_3Bi_4$, Sci. China Phys. Mech. Astron. **67**, 267411 (2024).

[31] L. Elcoro, B. Bradlyn, Z. Wang, M. G. Vergniory, J. Cano, C. Felser, B. A. Bernevig, D. Orobengoa, G. de la Flor, and M. I. Aroyo, *Double crystallographic groups and their representations on the Bilbao Crystallographic Server*, J. Appl. Crystallogr. **50**, 1457 (2017).

[32] I. D. Hughes, M. Däne, A. Ernst, W. Hergert, M. Lüders, J. Poulter, J. B. Staunton, A. Svane, Z. Szotek, and W. M. Temmerman, *Lanthanide contraction and magnetism in the heavy rare earth elements*, Nature (London) **446**, 650 (2007).

[33] Y. Tokura and N. Kanazawa, *Magnetic skyrmion materials*, Chem. Rev. **121**, 2857 (2021).

[34] Y. Dong, Y. Kinoshita, M. Ochi, R. Nakachi, R. Higashinaka, S. Hayami, Y. Wan, Y. Arai, S. Huh, M. Hashimoto, D. Lu, M. Tokunaga, Y. Aoki, T. D. Matsuda, and T. Kondo, *Pseudogap and Fermi arc induced by Fermi surface nesting in a centrosymmetric skyrmion magnet*, Science **388**, 624 (2025).

[35] B. R. Ortiz, H. Miao, D. S. Parker, F. Yang, G. D. Samolyuk, E. M. Clements, A. Rajapitamahuni, T. Yilmaz, E. Vescovo, J. Yan, A. F. May, and M. A. McGuire, *Evolution of highly anisotropic magnetism in the titanium-based kagome metals* $LnTi_3Bi_4$ $(Ln: La \cdots Gd^{3+}, Eu^{2+}, Yb^{2+})$, Chem. Mater. **35**, 9756 (2023).

[36] I. A. Campbell, *Indirect exchange for rare earths in metals*, J. Phys. F **2**, L47 (1972).

[37] D. Stornaiuolo, C. Cantoni, G. M. De Luca, R. Di Capua, E. Di. Gennaro, G. Ghiringhelli, B. Jouault, D. Marrè, D. Massarotti, F. Miletto Granozio, I. Pallecchi, C. Piamonteze, S. Rusponi, F. Tafuri, and M. Salluzzo, *Tunable spin polarization and superconductivity in engineered oxide interfaces*, Nat. Mater. **15**, 278 (2016).

[38] T. Nomoto, T. Koretsune, and R. Arita, *Formation mechanism of the helical Q structure in Gd-based skyrmion materials*, Phys. Rev. Lett. **125**, 117204 (2020).

[39] G. Kresse and J. Furthmüller, *Efficiency of ab-initio total energy calculations for metals and semiconductors using a plane-wave basis set*, Comput. Mater. Sci. **6**, 15 (1996).

[40] J. P. Perdew, K. Burke, and M. Ernzerhof, *Generalized gradient approximation made simple*, Phys. Rev. Lett. **77**, 3865 (1996).

[41] G. Pizzi *et al.*, *WANNIER90 as a community code: New features and applications*, J. Phys. Condens. Matter **32**, 165902 (2020).